Investigation on acoustic, thermal, and tribological properties of hydrodynamic journal bearing with heterogeneous rough/smooth surface

by Paryanto

Submission date: 13-Mar-2025 11:00AM (UTC+0700)
Submission ID: 2414762409
File name: namic_journal_bearing_with_heterogeneous_roughsmooth_surface.pdf (27.86M)
Word count: 13425
Character count: 69714

Results in Engineering 18 (2023) 101112

Contents lists available at ScienceDirect

Results in Engineering

journal homepage: www.sciencedirect.com/journal/results-in-engineering

Investigation on acoustic, thermal, and tribological properties of hydrodynamic journal bearing with heterogeneous rough/smooth surface

Mohammad Tauviqirrahman [a,*], Eflita Yohana [a], Paryanto [a,b], Jamari [a], Fauzan Syukri Muslim [a], Paulus Wisnu Anggoro [c]

[a] Laboratory for Engineering Design and Tribology, Department of Mechanical Engineering, Diponegoro University, Jl. Prof. Soedharto SH, Tembalang, Semarang, 50275, Indonesia
[b] Institute for Factory Automation and Production System (FAPS), Friedrich-Alexander-Universität Erlangen-Nürnberg, Egerlandstr.7-9, Erlangen, 91058, Germany
[c] Department of Industrial Engineering, Faculty of Industrial Technology, University of Atma Jaya Yogyakarta, Jl. Babarsari 44, Yogyakarta, 55281, Indonesia

ARTICLE INFO

Keywords:
Acoustic
Cavitation
Computational fluid dynamics (CFD)
Surface roughness
Thermohydrodynamic

ABSTRACT

High level of noise limits the reliability of the lubricated journal bearing. In the current paper, the possibility of bearing design with a heterogeneous rough/smooth surface is explored using the computational fluid dynamics (CFD) approach to improve tribological and acoustic performance. A parametric analysis is conducted to determine the optimal surface roughness level, the cavitation pressure, and the ratio of length to the diameter of the journal. The effect of the presence of a roughened pattern on the thermal behavior of the lubricant, friction force, noise level, and cavitation phenomena was also studied in depth. The main finding of the present study is that when conventional journal bearing fails in generating the load support for concentric conditions, the heterogeneous rough/smooth bearing has a beneficial effect by increasing the load-carrying capacity. Furthermore, the high level of surface roughness can significantly increase the load-carrying capacity while decreasing frictional forces and acoustic power. However, the roughness does not dramatically change the maximum temperature (less than 1%). The numerical results also suggest that the variation in vapor saturation pressure has a negligible effect on the maximum temperature, friction force, and noise level.

1. Introduction

In the industrial sector, journal bearings are the most commonly used types of hydrodynamic bearings due to some advantages such as ease of installation, minimal maintenance costs, and good damping capability despite their use under high loads, at high speeds, and with great accuracy and precision [1]. Rapid technical breakthroughs have occurred over the previous few decades, and the operating conditions of machines are becoming increasingly stringent, precise, and challenging. As a result, to achieve these requirements, it becomes critical that bearings be designed based on more realistic bearing characteristic data.

For plain journal bearings, the design approach typically begins with the selection of bearing dimensions such as the journal diameter (D), bearing length (L), and radial clearance (c). Initially, the load-carrying capacity of a plain bearing is more important to the designer, and this load-carrying capacity is mostly determined by the basic dimension, which is the journal diameter (D). A critical design decision is a length over diameter ratio (L/D). In comparison to a shorter bearing, a long bearing has a higher load capacity.

Many studies have been conducted to better understand the relationship between bearing dimensions and the performance of hydrodynamic journal bearings [2–4]. The most important result gained from their research was increasing the L/D of journal bearings increases the tribological performance of journal bearings in terms of load-carrying capacity by 10–1000% depending on the eccentricity ratio load-carrying capacity [4].

Numerous authors have expressed interest in a hydrodynamic journal that addresses cavitation, owing to the certainty connected with cavitation presence. Lin et al. [5] revealed that saturation pressure is a critical factor that must be taken into consideration during the numerical study of cavitation phenomena. In addition, it makes it possible for the hydrodynamic impact to become stronger and the cavitation region to become smaller, by increasing the saturation vapor pressure as a result of the expansion of the high-pressure zone and so weakening the cavitation zone. When the bearing pressure is high, regardless of how much the positive pressure can rise, the negative pressure cannot surpass

* Corresponding author.
E-mail address: mohammad.tauviqirrahman@ft.undip.ac.id (M. Tauviqirrahman).

https://doi.org/10.1016/j.rineng.2023.101112
Received 6 January 2023; Received in revised form 16 April 2023; Accepted 16 April 2023
Available online 20 April 2023

a specific limit. When the absolute value of the negative pressure reaches a particular value, the lubricating fluid film ruptures, preventing the pressure in the rupture area from lowering further [6]. In the case of textured journal bearing, Mao et al. [7] showed that the cavitation phenomenon may aid in improving the performance of hydrodynamic lubrication. Research demonstrated that under a parallel surface, the friction coefficient is at its lowest when the depth ratio is between 0.6 and 0.7, and it is even lower when the width ratio is between 0.7 and 0.8. Experimentally, in hydrodynamically lubricated parallel sliders, it was also observed that cavitation occurs within the structure, and that lubricant film thickness correlates strongly with cavitation [8]. According to Chen et al. [9], from the numerical perspective, the multiphase flow model is suitable for simulating cavitation because the maximum difference between simulation results and experimental data is less than 6%. Later, Dhande and Pande [1,10] revealed that the distribution of oil vapor continues to reduce by 40% the magnitude of pressure buildup in the bearing. Abbas et al. [11] also noted a similar finding. When bearings are operating at higher speeds, the multiphase study of bearings with cavitation becomes crucial. They reported that the percentage drop in maximum oil film pressure due to the cavitation effect is between 30 and 50% depending on the shaft rotational speed. In addition, numerous studies have demonstrated that the application of the multiphase model accurately predicts cavitation [12–16]. In a recent publication, Chen et al. [16] compared the multiphase model to the experiment and observed that the difference is less than 6%. Based on these studies, it is necessary to include cavitation effects with the multiphase approach when solving the lubrication problem to arrive at a solution that is acceptable for real-life conditions.

Because of the increased demand for high-speed machinery during the last few decades, the thermal effect has also taken center stage in the field of lubrication theory. It is actually more likely that a high-speed engine will cause the temperature distribution of the journal bearings to vary which is highly impacted by the viscosity of the lubricating fluid. In accordance with the findings of Li et al. [17], the viscosity of the lubricating fluid is greatly impacted by the fluid temperature. The viscosity of the lubricating fluid decreases with the increasing temperature of the lubricating fluid, which affects the performance of the journal bearing under load. Kyrkou and Nikolakopoulos [18] conducted a thermo-hydrodynamic analysis to predict the temperature distribution of the fluid in the bearing. One of their main findings was that for an isothermal bearing, the maximum temperature rises when the rotational speed is held constant and the external load is increased. In recent literature, Xiang et al. [19] developed a 3D transient thermal model combined with a profile modification design formula to incorporate the complicated multifield characteristics.

There is a manufacturing process using grinding in the production of bearings [20]. Grinding can be considered as an option for producing bearing components with a combination of low surface roughness, tight dimensional tolerances, and high lubricant retention capacity [21]. Workpieces that require a high level of surface quality and precise shape and dimensions are finished by grinding. This procedure changes the roughness of the bearing's outer and inner surfaces. The surface roughness has a significant impact on the bearing's properties. Using surface roughness to raise the thickness of the lubricating fluid coating on journal bearings has the potential to improve the lubrication performance of these bearings. It has been demonstrated that the introduction of surface roughness demonstrates the enhanced load-bearing capacity [22–26]. Bhaskar et al. [22] studied the characteristics of bearings with three various surface roughness orientations. They found that the load-carrying capacity of a bearing with longitudinal surface roughness is 52.57% more than that of an ideal smooth bearing with no surface roughness. Based on the Reynolds model, Kalavathi et al. [23] observed that the load-bearing capacity improves with surface roughness. Later, according to the experiment results, the surface roughness with a large negative skewness surface has the best lubricating performance [24]. Zhu et al. [25] found that when the surface roughness height increases, the load-carrying capacity enhances by 47.38%. Skaltsas et al. [26] revealed that the maximum pressure and load-carrying capability of a rough bearing both rise significantly, up to 14% and 10%, respectively. Similarly, Tomar and Sharma [27] demonstrated that bearing stability is improved by longitudinal surface roughness patterns.

In addition to the beneficial effect of increased load-carrying capacity brought about by surface roughness, it was also revealed that surface roughness can decrease friction parameters [26]. The friction parameters are reduced by a maximum of 1.2% compared to those of a smooth bearing. Baineni et al. [28] showed a similar result. Compared to a smooth surface, a rough surface with an isotropic roughness pattern produces less friction.

In general, according to a survey of the literature on the effect of surface roughness, numerous researchers have only focused on tribological performance. To the best of our knowledge, there is very little research on the effect of bearing surface roughness on acoustic performance. Due to the potential danger to the environment and hearing of the people posed by journal bearing noise (50–80 dB), it is important to highlight the early work of Othman et al. [29], who experimentally established that the sound pressure level is related to the surface roughness of the utilized material. Therefore, studying the effect of surface roughness on bearing noise becomes necessary and meaningful.

According to the classical lubrication theory, the parallel slider (i.e. concentric condition) cannot support the load due to the absence of the converging geometrical wedge to produce desirable hydrodynamic pressure. It is hypothesized that by selecting a pattern of rough/smooth zones, enhanced bearing features can be achieved even when the wedge effect is absent (i.e. zero eccentricity ratio). The present study examines the use of engineered surface roughness to enhance the performance of fluid-film bearings using utilizing the computational fluid dynamics (CFD) technique. By engineering a heterogeneous bearing surface with roughness in some areas but not in others, the flow pattern of the liquid lubricating surface can be adjusted. The concept of heterogeneous rough/smooth bearing proposed here is inspired by the capability of heterogeneous slip/no-slip bearing, which can give rise to a considerable hydrodynamic pressure [23,30–32] even in concentric conditions.

Generally speaking, evaluating the performance of concentric journal bearings with a heterogeneous rough/smooth surface under a variety of operating situations necessitates a mass-conserving approach. The phase change of the lubricant within the journal, suggesting cavitation, was not predicted by the single-phase study. Additionally, another feature that has been frequently overlooked in various research is the so-called viscosity wedge caused by temperature change, which results in the variation of lubricant viscosity within the lubricant domain. Thus, to achieve more realistic findings, the journal bearing with zero eccentricity ratio, which is equivalent to the parallel slider, is of great relevance in this section when the multiphase model is used and the temperature effect is considered. Here, the influence of the length over diameter ratio, vapor saturation pressure, and the level of surface roughness in relation to the tribological and acoustic performance of the journal bearing are all important considerations. The performance of journal bearings is determined by utilizing the computational fluid dynamics (CFD) technique, which entails running a series of simulations to determine their performance. Furthermore, the nominal operating condition for the shaft rotating speed of the journal bearing ranges from 1000 to 6500 rpm [33]. Since hydrodynamic lubrication is assumed in the present study, the rotational speed of the shaft chosen for analysis must be sufficient to prevent contact between mating surfaces. Therefore, in this work, the 2000 rpm is used for shaft rotational speed. Using surface roughness modeling, this work gives a detailed strategy for achieving the best tribological performance possible for journal bearings, which includes a high load-carrying capacity, low friction force, low acoustic power level, and good thermal characteristics.

2. Simulation method

2.1. Geometric model

All computational models in this study are based on the three-dimensional parametric design of journal-bearing systems. To illustrate the significance of the major parameters and the geometry of the computational domains, Fig. 1 depicts a schematic illustration of the journal bearing. The cylindrical journal with radius R_j revolves at a constant rotational speed relative to the bearing bushing with radius R_b. The difference between R_j and R_b is referred to as the radial clearance c. The eccentricity distance between the bearing's center (O_b) and the journal's center (O_j) is denoted by the symbol e. In practice, eccentricity exists as a result of the vertically applied load at the journal's center (O_j). The eccentricity ratio is defined as the ratio of eccentricity distance e to radial clearance c. The related simulation model parameters, including the geometric configuration and lubricant characteristics, are listed in Table 1.

This study introduces the concept of a heterogeneous rough/smooth bearing, in which the rough condition is applied to some areas while others remain smooth. The basic geometry of the heterogeneous rough/smooth used here as shown in Table 1 adopts the slip geometry of the heterogenous slip/no-slip bearing as presented by Cui et al. [31]. It has been demonstrated that this geometry increases the load-bearing capacity.

As discussed by Welsh [18], a good rule of thumb for designing the journal bearing is to keep the length over diameter ratio (L/D) between 0.5 and 1.5. A longer bearing, by definition, has a greater load-carrying capacity than a shorter bearing. A longer bearing, on the other hand, increases the probability of bearing failure due to misalignment errors.

Table 1
Parameters of the model.

Parameters	Value	Unit
Bearing		
Bearing diameter, D_b	50	mm
Bearing length, L_b	25; 50; 75	mm
Radial clearance, c	0.05	mm
Eccentricity ratio, ε	0	–
Attitude angle, φ	0	o
Rotational velocity, n	2000	rpm
Fluid		
Oil density, ρ	850	kg/m^3
Oil viscosity, μ	0.0125	Pa.s
Oil specific heat capacity C_p (40 °C)	1944	J/kg.K
Oil thermal conductivity λ (40 °C)	0.12789	W/m.K
Vapor density, ρ_v	10.95	kg/m^3
Vapor dynamic viscosity, μ_v	2×10^{-5}	Pa.s
Vapor saturation pressure, P_{sat}	3000; 15,000; 29,185; 30,000; 50,000	Pa
Vapor specific heat capacity C_{pv}	2430	J/kg.K
Vapor thermal conductivity λ_v	0.0178	W/m.K
Roughness Area		
Length of roughness area, L_R	78.657	mm
Roughness width, W_R	20; 40; 60	mm

Additionally, a longer bearing decreases the amount of fluid circulating inside, resulting in a higher peak temperature inside the lubrication film and on the bearing surface [35]. For this reason, in this study, the length over diameter ratio (L/D) is varied to 0.5, 1, and 1.5 as indicated in Table 1.

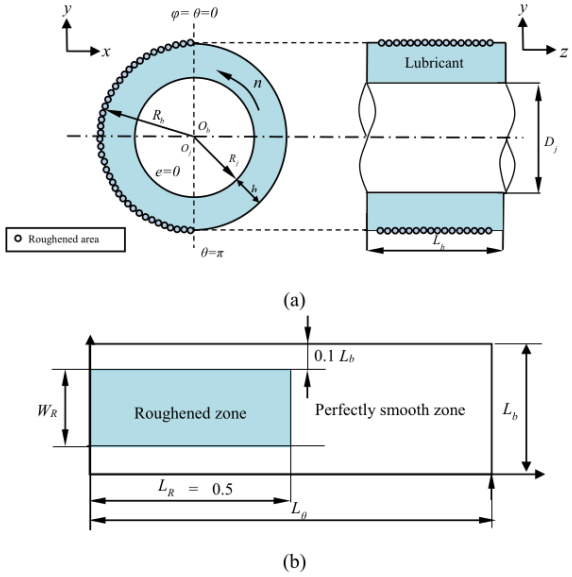

Fig. 1. Schematic diagram, (a) heterogeneous rough/smooth journal bearing, (b) heterogeneous rough/smooth pattern.

2.2. Meshing

To construct the lubricant film, in this study, hexahedral elements are used via the ANSYS ICEM-CFD module, which significantly improves computation efficiency and precision. To ensure the accuracy of the results, the sensitivity of grid density to load-carrying capacity is determined. To ensure satisfactory convergence, the refinement criteria, which specify the number of fluid layers with linear proportion in the radial direction, are specified. The radial grid is believed to be the most critical, as it must be capable of capturing the phenomena occurring within the film thickness. Each computation is carried out under identical operating conditions but with a different fluid layer division (and thus different mesh sizes). Note that for this independent mesh study, the bearing type chosen is a traditional smooth one (without engineered roughness), while the basic geometry and lubricant properties are as shown in Table 1, with the eccentricity ratio chosen to be 0.8 instead of zero. It is understandable because to prevent failure lubrication, the eccentricity ratio caused by wedge effect must be applied to traditional smooth bearings. In particular, the L/D ratio employed is 0.5, and the saturation vapor pressure of oil is 29,185 Pa.

The result of a grid-independent study in terms of maximum hydrodynamic pressure under various mesh layers is shown in Fig. 2 for two rotational speeds, i.e. $n = 2000$ and 4000 RPM. According to Fig. 2, the fluid layer division is determined after sensitivity analysis reveals that several layer division values (4, 5, and 7) change the maximum hydrodynamic pressure of the bearing by less than 2% in the CFD model both for the case of $n = 2000$ and 4000 RPM. To summarize, the 4-layer fluid domain division is used for all simulations because it combines a reasonable computational time with a feasible level of independent meshing. Based on this mesh configuration, a lubricant domain is generated for all bearings covered here, that is bearings with L/D of 0.5, 1, and 1.5. It means that the bearing length determines the number of cells along the axial direction. This results in the radial, circumferential, and axial directions being covered by the corresponding grid distribution, i.e. 4 x 400 x 40, 4 x 400 x 80, and 4 x 400 x 160, respectively, for the case of L/D of 0.5, 1 and 1.5 as depicted in Fig. 3.

2.3. Boundary condition

There are a number of boundary conditions provided for the simulation setting. The "pressure inlet" and "pressure outlet" are given in the computational lubricant domain with gauge pressure set to zero Pascal both for the inlet area and the outlet area. The stationary surface designates the housing wall, whereas the rotating shaft with a 2000 RPM rotational speed defines the journal area. There are no-slip criteria on the interface surfaces for velocity. For thermo-hydrodynamic

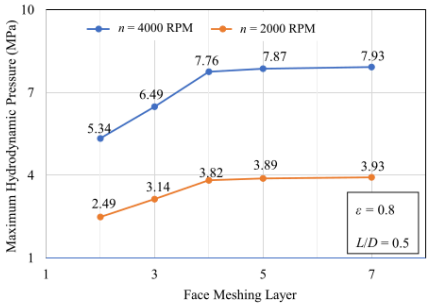

Fig. 2. Mesh independent study results.

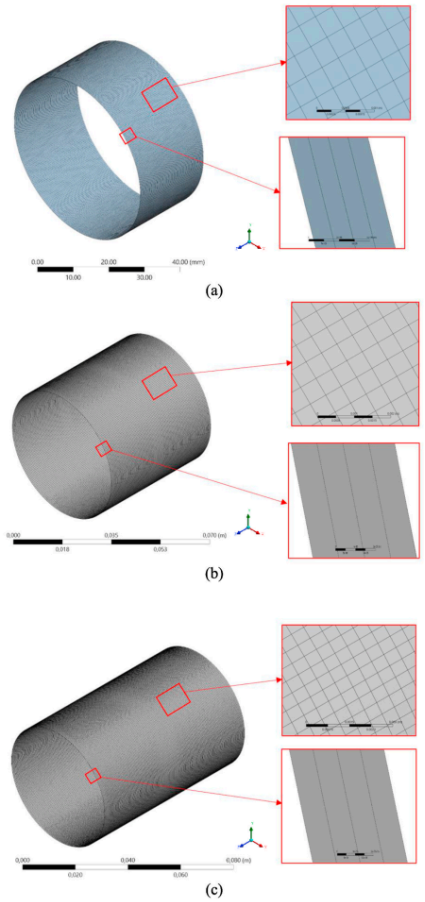

Fig. 3. Meshing of lubricant fluid domain for different values of L/D: (a) 0.5, (b) 1, and (c) 1.5.

conditions, the temperature inlet, as well as the temperature outlet, are set to 293 K. In detail, Fig. 4 shows the boundary conditions applied to the journal bearing.

2.4. Solution setup

In this simulation, the pressure-based solver and the SIMPLE pressure–velocity coupling method are used to quickly obtain results. For the momentum equations, the second-order upwind discretization scheme is employed, while for the volume fraction, the QUICK discretization scheme is used. In addition, the first-order upwind scheme is applied to

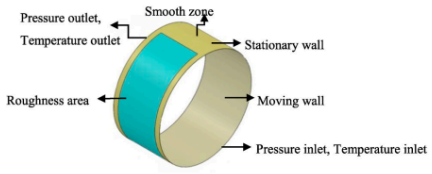

Fig. 4. Schematic of lubricant domain with boundary conditions.

discretize the turbulent kinetic energy and turbulent dissipation rate. In the present investigation, the convergence precision for pressure and energy is $1x10^{-5}$ and $1x10^{-6}$, respectively.

3. Theory

3.1. Governing equations

The lubricant flow, pressure formation, and heat dissipation in the flow domain were calculated using a CFD (computational fluid dynamics) model in this work. For a continuous fluid medium, the lubricant behavior is evaluated using the momentum and continuity equations from classical fluid mechanics.

The equation for mass conservation is as follows:

$$\frac{\partial}{\partial \mathbf{x_i}}(\boldsymbol{\rho}\mathbf{u_i}) = \mathbf{0} \tag{1}$$

In this work, the Reynolds-averaged Navier-Stokes (RANS) equations, in particular, are used to obtain the hydrodynamic lubrication pressure in order to quantify the bearing noise. It should be noted that the Reynolds decomposition, which includes the breakdown of an instantaneous quantity into its time-averaged and fluctuating components, is the primary technique for deriving the RANS equations from the instantaneous Navier-Stokes equations. The formulation for RANS equations reads [36]:

$$\frac{\partial}{\partial \mathbf{x_i}}(\boldsymbol{\rho}\mathbf{u_i}\mathbf{u_j}) = -\frac{\partial \mathbf{p}}{\partial \mathbf{x_i}} + \frac{\partial}{\partial \mathbf{x_j}}\left[\boldsymbol{\mu}\left(\frac{\partial \mathbf{u_i}}{\partial \mathbf{x_j}} + \frac{\partial \mathbf{u_j}}{\partial \mathbf{x_i}}\right)\right] + \frac{\partial}{\partial \mathbf{x_j}}\left(-\boldsymbol{\rho}\overline{\mathbf{u_i'}\mathbf{u_j'}}\right) \tag{2}$$

Here, $\boldsymbol{\rho}$ is the density; u_i and u_j are the average velocity components for the coordinate X, Y, and Z; p is the hydrodynamic pressure; μ is the viscosity; u'_i and u'_j are the fluctuation velocities; $i, j = 1, 2, 3$ (x, y, z); and $-\boldsymbol{\rho}\overline{\mathbf{u_i'}\mathbf{u_j'}}$ is the Reynolds stress and expressed as:

$$-\boldsymbol{\rho}\overline{\mathbf{u_i'}\mathbf{u_j'}} = \boldsymbol{\mu}\left(\frac{\partial \mathbf{u_i}}{\partial \mathbf{x_j}} + \frac{\partial \mathbf{u_j}}{\partial \mathbf{x_i}}\right) - \frac{2}{3}\left(\boldsymbol{\rho}\mathbf{k} + \boldsymbol{\mu_t}\frac{\partial \mathbf{u_i}}{\partial \mathbf{x_i}}\right)\boldsymbol{\delta_{ij}} \tag{3}$$

where the temporal average of the product of the fluctuating velocities is represented by the overbar. δ_{ij} is addressed to the Kronecker delta symbol. If $i \neq j$, $\boldsymbol{\delta_{ij}} = 0$. If not, $\boldsymbol{\delta_{ij}} = 1$. The symbol μ_t refers to the turbulent viscosity coefficient and is defined as $\mu_t = C_\mu \rho k^2/\varepsilon_d$. Here, C_μ is devoted to the turbulent constant and set to 0.09 [36] while k and ε_d, respectively, refer to the standard turbulent kinetic energy and turbulent dissipation rate, whose definitions are expressed below:

$$\mathbf{k} = \frac{\overline{\mathbf{u_i'}\mathbf{u_j'}}}{\mathbf{2}} \quad \textbf{and} \quad \boldsymbol{\varepsilon_d} = \frac{\boldsymbol{\mu}}{\boldsymbol{\rho}}\left(\overline{\frac{\partial \mathbf{u_i'}}{\partial \mathbf{x_j}}\frac{\partial \mathbf{u_i'}}{\partial \mathbf{x_j}}}\right) \tag{4}$$

It should be noted that the values of the parameters k and ε_d indicate how much fluid turbulence is responsible for the bearing noise. In this work, a standard k-ε_d model is used to determine the values of k and ε_d in accordance with the equation suggested by Launder and Spalding [37] (given in Eq. (5) below). The Boussinesq hypothesis serves as the foundation for this model.

$$\frac{\partial}{\partial \mathbf{x_i}}(\boldsymbol{\rho}\mathbf{k}\mathbf{u_i}) = \frac{\partial}{\partial \mathbf{x_j}}\left(\boldsymbol{\mu} + \frac{\boldsymbol{\mu_t}}{\boldsymbol{\sigma_k}}\right)\frac{\partial \mathbf{k}}{\partial \mathbf{x_i}} + \left[\boldsymbol{\mu_t}\frac{\partial \mathbf{u_j}}{\partial \mathbf{x_i}}\left(\frac{\partial \mathbf{u_i}}{\partial \mathbf{x_j}} + \frac{\partial \mathbf{u_j}}{\partial \mathbf{x_i}}\right)\right] - \boldsymbol{\rho}\boldsymbol{\varepsilon_d} \tag{5a}$$

$$\frac{\partial}{\partial \mathbf{x_i}}(\boldsymbol{\rho}\boldsymbol{\varepsilon_d}\mathbf{u_i}) = \frac{\partial}{\partial \mathbf{x_j}}\left(\boldsymbol{\mu} + \frac{\boldsymbol{\mu_t}}{\boldsymbol{\sigma_{\varepsilon_d}}}\right)\frac{\partial \boldsymbol{\varepsilon_d}}{\partial \mathbf{x_i}} + \left[\mathbf{C_1}\boldsymbol{\mu_t}\frac{\boldsymbol{\varepsilon_d}}{\mathbf{k}}\frac{\partial \mathbf{u_j}}{\partial \mathbf{x_i}}\left(\frac{\partial \mathbf{u_i}}{\partial \mathbf{x_j}} + \frac{\partial \mathbf{u_j}}{\partial \mathbf{x_i}}\right)\right] - \mathbf{C_2}\boldsymbol{\rho}\frac{\boldsymbol{\varepsilon_d^2}}{\mathbf{k}} \tag{5b}$$

Based on reference [32], the empirical values of C_1, C_2, σ_k, and σ_{ε_d} are assumed to be 1.44, 1.92, 1.0, and 1.3, respectively. After calculating the hydrodynamic pressure using Eq. (5), the load-carrying capacity of the bearing W may be determined from the integration of the hydrodynamic pressure acting on the bearing surface. It reads:

$$\mathbf{W} = \iint_{\mathbf{A}} \mathbf{p}\mathbf{r}\boldsymbol{\theta}\mathbf{d}\boldsymbol{\theta}\mathbf{d}\mathbf{z} \tag{6}$$

where θ represents the circumferential angle. The following is an expression for the frictional force f caused by the viscosity shear force of the lubricant acting on the shaft:

$$\mathbf{f} = -\iint \boldsymbol{\tau}\mathbf{r}\mathbf{d}\boldsymbol{\theta}\mathbf{d}\mathbf{z} \tag{7}$$

In fact, the viscosity of lubricant fluids is significantly influenced by the fluid temperature. The higher the fluid temperature, the lower the viscosity value, and this tends to affect the ability of the journal bearing to withstand load. Thus, heat transfer is considered in this work, and consequently, an additional equation for energy conservation is solved. The temperature through the lubricating film layer is interpreted as energy conservation. It reads:

$$\boldsymbol{\rho}\mathbf{C_p}\mathbf{V}.\nabla\mathbf{T} = \nabla.(\boldsymbol{\lambda}\nabla\mathbf{T}) - \boldsymbol{\tau} : \nabla\mathbf{V} \tag{8}$$

where C_p denotes the liquid-specific heat capacity, T is the liquid temperature, and λ refers to liquid thermal conductivity.

3.2. Viscosity modeling

Due to the sensitivity of temperature, it is critical to address the viscosity values that fluctuate with rising temperature in various types of lubricant applications [38,39]. In this work, the Walther viscosity relation was used to demonstrate the viscosity variation with temperature [17,38,39].

$$\mathbf{log\ log}\ (\mathbf{v} + \mathbf{0.7}) = \mathbf{10.0032} - \mathbf{3.9785}\ \mathbf{log\ T} \tag{9}$$

The variation in other characteristics as a function of temperature is defined by

$$\begin{aligned} \boldsymbol{\rho} &= \boldsymbol{\rho}_{\mathbf{15.6}}[\mathbf{1} - \mathbf{0.00063}(\mathbf{T} - \mathbf{15.6})] \\ \mathbf{C_p} &= \mathbf{1.800}(\mathbf{1} + \mathbf{0.002T}) \\ \boldsymbol{\lambda} &= \mathbf{0.1312}(\mathbf{1} - \mathbf{6.3} \times \mathbf{10^{-4}T}) \end{aligned} \tag{10}$$

where v is the kinematic viscosity, T is the temperature, ρ is density, C_p is specific heat, and λ is the thermal conductivity of the lubricant. For all following computations, to incorporate the viscosity modeling as a function of temperature as shown in Eq. (4), the polynomial profile which is available in ANSYS FLUENT was employed [36].

3.3. Surface roughness modeling

Many roughness parameters are used to characterize surface roughness. However, the roughness average (R_a) is the most commonly used parameter [40] and it is defined as follows:

$$\mathbf{R_a} = \frac{\mathbf{1}}{\mathbf{n}}\sum_{\mathbf{i=1}}^{\mathbf{n}}|\mathbf{y_i}| \tag{11}$$

where y_i is the distance from the average height of a profile for

measurement i, and n denotes the number of measurements. In this work, the sand-grain model, as illustrated in Fig. 5, is used to characterize the roughness profile of the rough surface of a heterogeneous rough/smooth bearing. The sand-grain model was demonstrated experimentally and numerically to accurately model real product roughness [41]. Furthermore, the sand grain model was appropriate for Reynolds-Average-Navier-Stokes (RANS) simulation, which is used here. In this model, a dense monolayer of spheres of diameter K_s is used to uniformly cover the surface. The modified law-of-the-wall for mean velocity is used to represent the surface roughness. This equation is as follows [36]:

$$\frac{u_p u^*}{\tau_w/\rho} = \frac{1}{\kappa}\ln\left(E\frac{\rho u^* y_p}{\mu}\right) - \Delta B \tag{12}$$

where $u^* = C_\mu^{1/4} k^{1/2}$ and $\Delta B = (1/\kappa)\ln f_r$. For sand-grain roughness, ΔB is affected by the physical roughness height K_s, while the height is assumed constant per surface [36].

It should be remembered that K_s is the corresponding sand grand roughness height, not the geometric roughness height of the surface. As a result, a conversion factor is required to convert the geometric roughness height of the surface to an equivalent sand-grain roughness. In this work, the R_a parameter, as illustrated in Fig. 1(b), is used to describe the roughness height K_s (Fig. 1(a)). R_a is the arithmetic mean of the roughness profile, which is measured by the profilometer.

The R_a value will be used as an input for all subsequent computations to indicate the roughness level of the heterogeneous rough/smooth bearing. According to the experiment of Adams et al. [40], the correlation between K_s and R_a can be characterized as follows:

$$K_s = 5.853\ R_a \tag{13}$$

As a note, depending on how much grinding was done, the surface roughness can be classified as precision (R_a = 0.1–0.2 μm), fine (R_a = 0.4–0.8 μm), medium (R_a = 1.6–6.3 μm), and rough (R_a = 12.5–100 μm) according to JIS B 0601–2013 [42]. Thus, in this work, to meet the possible range of surface roughness, four surface roughness classes will be selected for subsequent calculations, that is, namely R_a = 0.2 μm (precision), 0.8 μm (fine), 3.2 μm (medium), 12.5 μm (rough), and 15 μm (rough).

It should be noted that to maintain the bearing in hydrodynamic lubrication, the roughness height here must not exceed the minimum film thickness. Here, in our research, the highest roughness height (i.e. R_a) is 15 μm, while the minimum film thickness is 50 μm (Table 1). It means that the heterogeneous rough/smooth surface is effective when the surface roughness level R_a of the roughened area of bearing is much lower than the minimum film thickness h_{min} as employed in the present study.

3.4. Cavitation modeling

Cavitation is the process of rupturing a liquid by a reduction in pressure at a constant temperature [36,43]. In practice, the cavitation phenomena occur in the lubricant domain. In the lubrication problem, cavitation is the main issue that needs to be properly modeled. For all of the computations performed in this study, cavitation is modeled using a "mixture" model provided by the CFD software [36]. The pressure change generates the cavitation results. The mixture model describes two-phase vapor–liquid flow by assuming that the liquid phase transitions to the vapor phase when the film pressure low to less than the saturation pressure. To specify the dispersed phases, the mixture model solves the mixture equation and imposes relative velocities. The mixture model is a reduced version of the full multiphase model with a lower computational cost [44]. In this way, calculations are made on the growth of gas bubbles, which frequently accompany the cavitation phenomenon.

In the cavitation phenomena, the liquid–vapor mass transfer equation (i.e., evaporation and condensation) can be expressed as follows [36,45]:

$$\nabla\cdot\left(\alpha_v\rho_v\vec{V}\right) = R_g - R_c, \tag{14}$$

where α_v is the volume fraction of vapor and ρ_v is the density of vapor in lubricant. During cavitation, R_g and R_c are responsible for vapor generation and condensation rates. The Rayleigh-Plesset correlation is used to characterize the dynamics of a single spherical vapor bubble in a liquid [12,46]. For mixture flow analysis, in this study, the Zwart-Gerber-Belamri model [45] is used during the computations because it requires less computational effort than other multiphase cavitation models [36]. For the Zwart–Gelber–Belamri model, since all of the bubbles in a system are assumed to be the same size, the cavitation takes the following final form [36,45]:

$$\text{if } p \le P_{sat},\ R_g = F_{evap}\frac{3\alpha_{nuc}(1-\alpha_v)\rho_v}{R_B}\sqrt{\frac{2}{3}\frac{P_{sat}-p}{\rho}} \tag{15}$$

$$\text{If } p \ge P_{sat},\ R_c = F_{cond}\frac{3\alpha_v\rho_v}{R_B}\sqrt{\frac{2}{3}\frac{p-P_{sat}}{\rho}} \tag{16}$$

where F_{vap} is the evaporation coefficient with a value of 50, F_{cond} is the condensation coefficient with a value of 0.001, R_B is the bubble radius with a value of 10^{-6} m, and α_{nuc} is the nucleation site volume fraction with a value of 5×10^{-4}.

3.5. Noise modeling

The bearing noise is of special significance in the acoustic investigation presented here. The turbulence in the lubricant causes noise during bearing operation. The broadband noise source model is used in this work to solve the noise level created in the lubricant [36]. In the acoustic analysis, the acoustic performance of the bearing is represented by two terms: the acoustic power level and the average acoustic power level. The acoustic power level per unit volume P_A is given here based on the formula derivation of Lilley [47]. It reads:

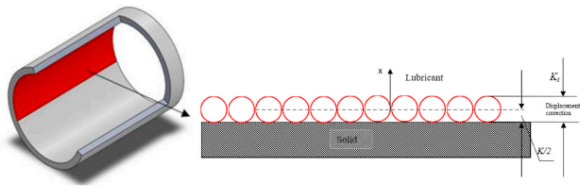

Fig. 5. Illustration of equivalent sand-grain roughness.

$$P_A = a_\varepsilon \rho \left(\frac{u_i^3}{l}\right) \frac{u_i^5}{a_0^5} \quad (17)$$

where a_ε is turbulence constant and is set to be 0.1 [36], while u_i and l are turbulence velocity and length scales, respectively and a_0 is the speed of the sound. Furthermore, Eq. (17) can be reduced in terms of k and ε_d as follows:

$$P_A = a_\varepsilon \rho \varepsilon_d \left(\frac{\sqrt{2k}}{a_0}\right)^5 \quad (18)$$

It should be acknowledged that the human hearing threshold, P_{ref} is 10^{-12} W/m^3 [33,36]. In this way, the bearing noise is associated with the lowest human threshold in terms of the acoustic power level P_{AL} that exists in the fluid. It reads:

$$P_{AL}(\mathrm{dB}) = 10 \log\left(\frac{P_A}{P_{ref}}\right) \quad (19)$$

Integrating the acoustic power level over the surface area yields the average acoustic power level. The acoustic power level can be derived from Equations (18) and (19) using the FLUENT module, while the average acoustic power level can be obtained by post-processing CFD results.

4. Results and discussion

4.1. Validation

Validation is a term that refers to the process of determining the accuracy of a methodology by comparing numerical results to published experimental/numerical data collected under the same conditions. The validation was carried out by comparing the present simulations to the studies of Dhande and Pande [1,10]. Figs. 6 and 7 depict the comparison between the pressure values generated by these authors [1,10] and the present investigation. The validated parameter is the maximum pressure value generated by the journal bearing at an eccentricity ratio of 0.8. Furthermore, the maximum pressure value obtained in the simulation conducted by Dhande and Pande [1,10] is 7.764 MPa for the case of the rotational speed of 4000 rpm and eccentricity ratio of 0.8. Based on Figs. 6 and 7, it can be revealed that the maximum pressure value obtained from the simulation of the current study is 7.752 MPa, representing an error of 0.15%. It implies that the method employed here is credible and accurate for the next simulations because it accurately identifies the hydrodynamic characteristics.

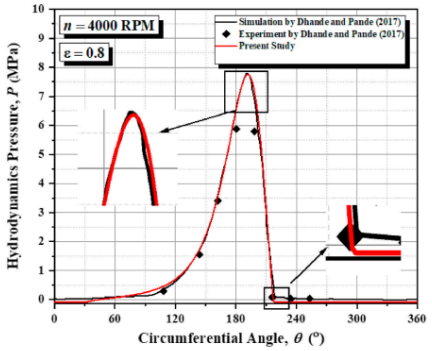

Fig. 6. Comparison of hydrodynamic pressure for journal bearings at $\varepsilon = 0.8$ between Dhande and Pande [1,10] with the present study. All results are evaluated at the mid-plane of the bearing ($z/L_b = 0.5$).

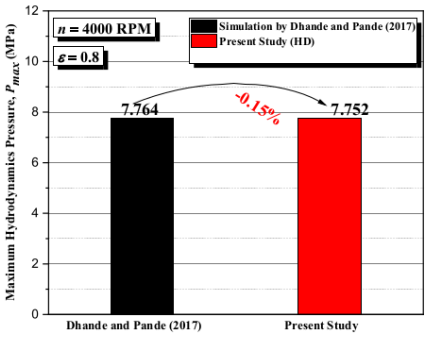

Fig. 7. Comparison of the maximum pressure for journal bearings at $\varepsilon = 0.8$ between Dhande and Pande [1,10] with the present simulation.

4.2. Effect of length to diameter (L/D) ratio

The effect of the L/D on the journal bearing with surface roughness modeling on the tribological performance of the journal bearing is obtained by varying the L/D. This section focuses on the bearing characteristics of pressure, wall temperatures, load-carrying capacity, average acoustic power level, friction force, and cavitation areas. This simulation was evaluated at zero eccentricity ratio, saturation pressure (P_{Sat}) of 29,185 Pa, surface roughness (R_a) of 12.5 μm, and a shaft rotational speed (n) of 2000 rpm.

Fig. 8 shows the histogram of the maximum pressure of the journal bearing with a heterogeneous rough/smooth pattern. It can be observed that an increase in the L/D increases the maximum pressure P_{max}. For the L/D considered here, the enhancement of the maximum pressure is significant. For example, the increase in P_{max} may be 12.59% if the L/D is tripled from 0.5 to 1.5. This is expected because a greater L/D will increase the contact area. The findings of this study are consistent with

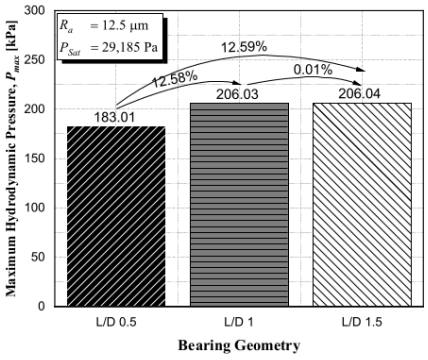

Fig. 8. Maximum pressure for several length-over-diameter ratios (L/D).

those obtained by Zhang et al. [2].

Fig. 9 depicts the results of the maximum lubricant temperature for various values of the L/D evaluated for both the moving and stationary walls. The simulation results show that the maximum lubricant temperature of the roughened journal increases as the L/D increases. However, unlike the maximum pressure trend, an increase in maximum temperature is not as significant, being less than 3%. The most likely explanation for why the L/D does not have a significant effect on the temperature rise is that the enlarged roughness area caused by an increased L/D causes a significant increase in leak flow, which prevents the temperature of the film from increasing. This is understandable because the longer the bearing, the more difficult it is to get adequate oil flow through the passage between the journal and the bearing. From Fig. 9, it is worth also noting that the values of the maximum temperature evaluated for moving and stationary walls have nearly identical values.

Fig. 10 shows the load-carrying capacity, friction force, and average acoustic power level at different L/D values. It can be revealed from Fig. 10(a) that the increase in L/D leads to a rise in the load-carrying

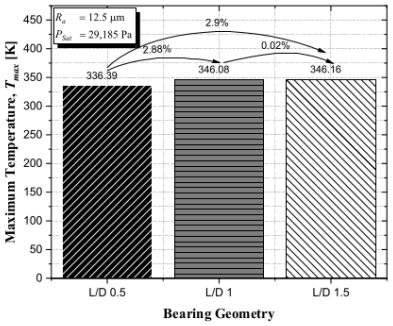

(a)

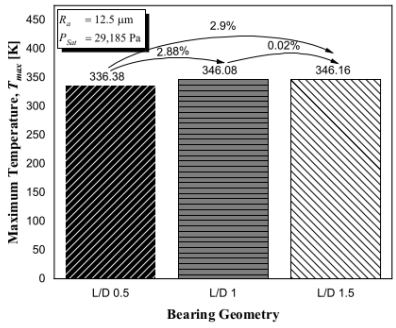

(b)

Fig. 9. Comparison of the maximum temperature varying length over diameter ratio (L/D) evaluated at (a) the moving wall, and (b) the stationary wall.

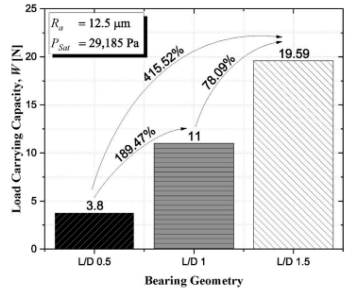

(a)

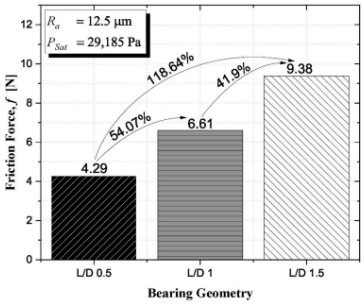

(b)

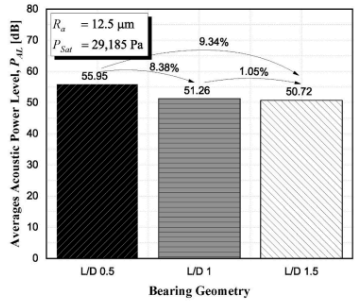

(c)

Fig. 10. Comparison of bearing performance with variation in length over diameter ratio (L/D) in terms of (a) load-carrying capacity, (b) friction force, and (c) average acoustic power level.

capacity. These results are consistent with the work carried out by Zhang et al. [2,3], and Maharshi et al. [4]. Another effect of increasing the L/D is the increased friction force, as depicted in Fig. 10(b). Concerning the acoustic performance of journal bearing with heterogeneous rough/-smooth bearing, the average acoustic power level is presented in Fig. 10 (c) for several values of L/D. An interesting result is found in Fig. 10 (c), that is, a decrease in the average acoustic power level by increasing the L/D is highlighted.

To investigate how large the area of the vapor phase formed in the bearing is, it is necessary to introduce the cavitation area. In this work, the percentage of cavitation area is calculated by dividing the area where the vapor phase forms by the area where the lubricant is still in its initial phase (i.e. liquid). Fig. 11 depicts the percentage of cavitation area of the roughened journal bearing. As expected that the cavitation area increases with increasing the L/D.

To explain in detail why the length over diameter ratio (L/D) has a significant effect on altering the journal bearing behavior, the contours of the pressure are presented for several values of L/D in Fig. 12. As reflected in Fig. 12, the pressure distribution pattern in the axial direction is similar for all values of L/D. It makes sense because, according to the principle of momentum conservation, the lubricant tends to create more momentum in the direction of the shaft's rotation. For this reason, increasing the length of the bearing does not significantly change the pressure characteristics in the axial direction. It can be observed that the maximum pressure at each variation occurs at the same circumferential angle, which is 180°. What distinguishes between variations is that in the circumferential direction, the low-pressure area increases with the increasing L/D.

Figs. 13 and 14 show the contours of the volume fraction of vapor evaluated either in the stationary or moving walls. For two walls, it can be seen that as the L/D increases, the cavitation area gets larger. It indicates that the vapor phase becomes larger when the L/D is increased.

Fig. 15 shows the pressure distribution and the volume fractions of vapor varyingthe length over diameter ratio. The results are evaluated at the mid-plane of the bearing(z/L_b = 0.5). By observing the pressure distribution, it is revealed that the maximumpressure at each variation occurs around the circumferential angle θ of 180°, which is thelocation of the edge between the roughened area and the smooth area. It is also foundthat the minimum pressure area increases with increasing the L/D. The circumferentialangle ranges from 0° to78° for the case of L/D = 0.5, 0° to 125° for the case of L/D = 1),and (0° to 137° for the case of L/D = 1.5. As a note, due to the multiphase cavitationmodel employed here, the minimum pressure achieves saturation pressure, which is29,185 Pa. When the pressure drop reaches a value below its saturated vapor pressure,the phenomenon of cavitation occurs. As a result, at a circumferential angle of 0° in eachvariation, a rupture occurs, and the fluid transitions from liquid to vapor. Reformationoccurs at circumferential angles of 78° (for L/D = 0.5), 126° (for L/D = 1), and 138° (for L/D = 1.5), where the fluid changes from vapor to liquid. Based on Fig. 15 (a), it can alsobe highlighted that increasing the L/D leads to a rise in the pressure peak. This result issimilar to the work of Zhang et al. [2]. Fig. 15(a) also shows that for the case of L/D =1.5, the pressure profile, particularly in the divergent area, appears to be larger than for L/D = 1. This feature results in a greater load-carrying capacity for L/D = 1.5 than for L/D = 1, as depicted in Fig. 10 above, although both have the same peak pressure,

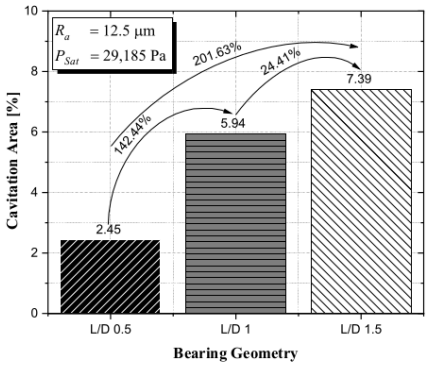

Fig. 11. Cavitation area as a function of length over diameter ratio (L/D).

Concerning the cavitation phenomena, Fig. 15 (b) and 15 (c) reveal that thevolume fraction of vapor reaches the peak in the circumferential angle range of 0°-10°. However, in the circumferential angle ranges of 0°-80° (for L/D = 0.5), 0°-128° (for L/D= 1), and 0°-140° (for L/D = 1.5), there is a difference in the volume fraction of vaporbetween both walls due to the presence of surface roughness on the stationary wall. Thisresult is consistent with the findings of Meng et al. [48], who found that the presence oftexture or roughness leads to the shrinking of the cavitation area in the journal bearing.Furthermore, Fig. 15 (b) and 15 (c) show that at circumferential angles of 80° (for L/D = 0.5), 128° (for L/D = 1), and 140° (for L/D = 1.5), the length of the area wherecavitation occurs increases with increasing L/D. This is caused by variations in the L/D, as shown in Figs. 13 and 14.

Fig. 16 illustrates the lubricant temperature distribution as assessed on the stationary and moving walls with varying L/D. It can be seen that the temperature peaks at the same circumferential angle range, i.e. θ of 0°–10° for both walls. The numerical results also indicate that increasing the L/D will increase the temperature profile both for the stationary and moving walls. However, for higher L/D, that is, in the case of L/D = 1 and 1.5, such an increase is not so significant. In addition, in particular in the case of the stationary wall, when the temperature reaches its peak, the (partial) surface roughness boundary conditions at an angle of 0°–180° in the stationary wall of the journal bearing produce a trend difference with the moving wall.

Fig. 17 (a), 17 (b), and 17 (c) show the acoustical indicators of the journal bearing in terms of the acoustic power level, turbulent eddy dissipation, and turbulent kinetic energy, respectively varying the L/D. All indicators are evaluated at the midplane (z/L = 0.5). Based on Fig. 17, it can be observed that due to the presence of surface roughness boundary conditions, there is a very small noise value between 27.5 and 37.5 dB in the circumferential angle range θ of 0° to 180° for all values of L/D. This phenomenon is explained by analyzing the turbulent velocity of lubricant. It seems that when the specific zone of the surface has a high level of surface roughness, turbulence is less likely to occur. It is more clear when the noise parameters are explored as depicted in Fig. 17 (b) and (c). This result is in good agreement with the finding of Meng et al. [33,48], which stated that the presence of texture or roughness reduces the value of turbulent kinetic energy and eddy dissipation produced by journal bearing. Furthermore, for all L/D, the values of turbulent eddy dissipation and turbulent kinetic energy are higher in the smooth area of the bearing than in the rough area. From Fig. 17, it can also be revealed that increasing the L/D reduces the acoustic indices. This result also explains why, as shown in Fig. 10(b) above, the average acoustic power level rises as the L/D value increases.

It should be mentioned that rather than focusing on the axial direction, the current study is more interested in exploring the bearing performance indicators in the circumferential direction. This is because, according to the direction of shaft rotation, the maximum gradient of pressure, temperature, and acoustic occur in the circumferential direction. However, to provide a comprehensive guideline for the design of a roughened bearing, it will be necessary to investigate the bearing performance indices in the axial direction in future research.

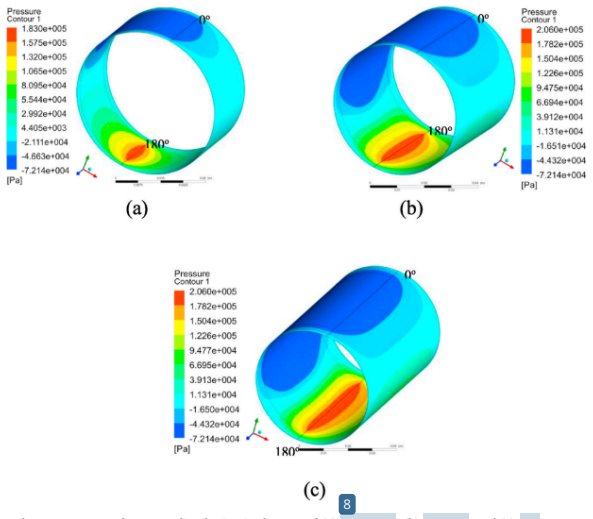

Fig. 12. Contour of pressure distribution in the case of (a) $L/D = 0.5$, (b) $L/D = 1$, and (c) $L/D = 1.5$.

4.3. *Effect of saturation pressure*

If the local hydrodynamic pressure drop causes the fluid pressure to fall below the saturation vapor pressure, the lubricant will begin to rupture. This occurrence is known as cavitation. In this section, the effect of saturation pressure on the performance of journal bearing with heterogeneous rough/smooth pattern is studied. The saturation pressure is varied for all subsequent simulations by 3 kPa, 15 kPa, 30 kPa, and 50 kPa. It is noted that from reference, for example in Ref. [49], the saturation pressure for oil has an average value of 2.34 kPa. For this reason, the saturation pressure for simulation begins at 3 kPa, and is then magnified by several factors up to 50 kPa. According to our hypotheses, the effect of the saturation pressure can be seen in more detail by increasing the interval of the variation in the saturation pressure, as Lin et al. [5] observed. Fig. 18 shows the effect of the saturation pressure on the maximum pressure. It can be observed that as the saturation pressure value increases in the journal bearing, it leads to a decrease in the hydrodynamic pressure. This is in line with the findings of Lin et al. [5], who found that the hydrodynamic pressure generated by journal bearings decreases as the saturation pressure value increases.

Fig. 19 shows the effect of saturation pressure on the predicted maximum temperature. The numerical results indicate that the resulting temperature decreases with increasing saturation pressure. The most likely explanation for this phenomenon is that multiphase cavitation flow was integrated with vapor cavitation in the present study. When the saturation pressure is decreased, vaporization (i.e., the formation of bubbles in the lubricant) becomes more pronounced, resulting in an increase in oil film temperature. This decrease, however, is not significant even when the saturation pressure is increased by a factor of 15. It can be seen from Fig. 19, that the decrease in maximum temperature is smaller than 3%. This holds true regardless of whether the lubricant temperature is calculated on the moving or stationary wall. It indicates that the cavitation phenomenon does not correspond well with the lubricant temperature from a physical standpoint. This is expected because cavitation is the process of rupturing a liquid by a reduction in pressure at a constant temperature [43].

To explore the effect of saturation pressure on the bearing performances, Fig. 20 shows the load-carrying capacity, friction force, and average acoustic power level. It can be seen that the load-carrying capacity generated by the journal bearing increases along with a rise in saturation pressure. Moreover, friction as well as the average acoustic power level exhibits an identical trend. The increase in saturation pressure has a positive effect in increasing the load-carrying capacity up to 40%. In reality, this means that the selection of lubricants for bearing journals that have high saturation pressure is quite crucial to maintaining load-bearing performance. Although it is not very significant (less than 5%), Fig. 20 also shows that an increase in saturation pressure can cause an increase in frictional force. An increase in average power level, which results in increased noise level, is another unfavorable consequence of rising saturation pressure. However, this rise in noise levels is only a 3% increase. According to these findings, saturation pressure appears to have a significant impact on load-carrying capacity.

Fig. 21 depicts the evaluated cavitation area on the moving and stationary walls. According to Fig. 21, the cavitation area increases as the saturation pressure increases. The increase in saturation pressure caused the cavitation area of the moving and stationary walls to increase by 73.04 and 75.52%, respectively. Although the percentage increase in the cavitation area on the moving wall is less than that of the stationary wall, the cavitation area on the moving wall is greater. Since the stationary wall area is subject to the boundary conditions of surface roughness, it influences the cavitation phenomenon.

Fig. 22 depicts the hydrodynamic pressure distribution and the volume fraction of the vapor evaluated on the stationary and moving walls. It can be seen that regardless of the P_{sat} value of the lubricant, the maximum pressure always occurs at the boundary side of the rough to smooth transition zone, that is, at $\theta = 180°$. Additionally, as the saturation pressure rises, the zone of the minimum pressure increases as well. From the physical point of view, a lubricant rupture takes place in this region, causing the fluid to transition from liquid to vapor. Furthermore, based on Fig. 22 (a), it can be revealed that with an

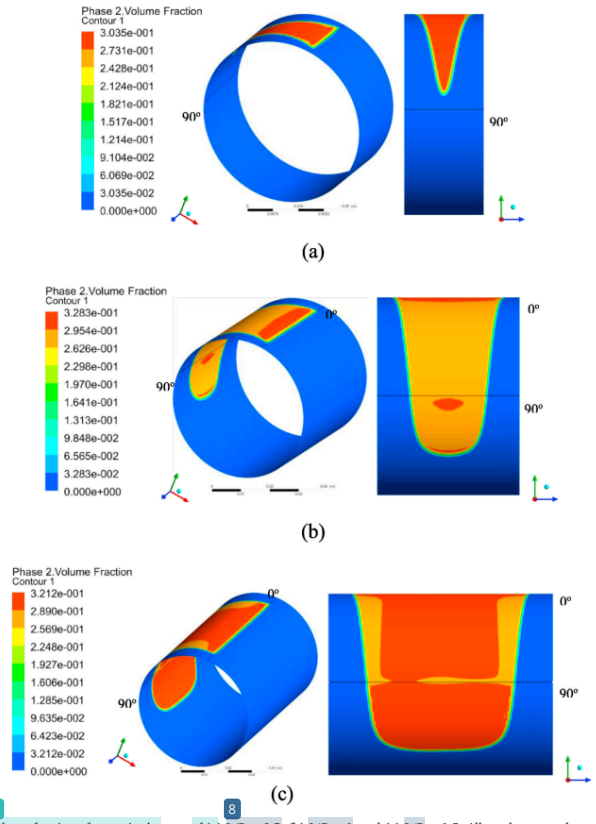

Fig. 13. Contour of volume fraction of vapor in the case of (a) $L/D = 0.5$, (b) $L/D = 1$, and (c) $L/D = 1.5$. All results are evaluated on the stationary wall.

increase in the journal bearing's saturation pressure value, the hydrodynamic pressure value decreases. This is consistent with the study conducted by Lin et al. [5]. Fig. 22 (b) and 22 (c) show that the volume fraction of vapor between stationary and moving walls reaches a maximum in the 0°–10° circumferential angle range. It is worth noting that the volume fraction of vapor differs slightly between moving and stationary walls. This is due to surface roughness in the stationary wall of the journal bearing at an angle of 0°–180°. As a result, the cavitation zone is smaller at the stationary wall than at the moving surface. Furthermore, based on Fig. 22 (b) and 22 (c), the results show that as the saturation pressure decreases, the area of cavitation decreases, indicating that some areas are not filled with lubricant. As a result, bubbles form in the lubricating fluid, lowering hydrodynamic pressure and influencing noise, friction, and load-bearing performance.

Fig. 23 shows the distribution of lubricant temperature varying saturation pressure P_{sat} evaluated at (a) the moving wall, and (b) the stationary wall. Based on Fig. 23, it can be observed that the larger the saturation pressure P_{sat}, the smaller the temperature distribution is. This prevails in both stationary and moving walls. For each P_{sat} condition, the temperature distribution in the convergent zone where a rough surface is applied to the journal bearing is greater than the temperature in the diverging region.

Fig. 24 (a), 24 (b), and 24 (c) reflect the profile of acoustic indices (i.e. acoustic power level, turbulent eddy dissipation, and turbulent kinetic energy) of the journal bearing with heterogeneous rough/smooth pattern with roughness level R_a of 12.5 μm. As can be seen, the acoustic power level decreases as saturation pressure decreases. As previously stated, this occurs due to a decrease in cavitation area with decreasing saturation pressure. Because of the presence of bubbles in the liquid, some areas are not filled with lubricant when cavitation occurs. Such a location may generate noise. Fig. 24 (b) and 24 (c) show the distribution of turbulent dissipation rate and turbulent kinetic energy. According to Fig. 24, as the saturation pressure ratio rises, both turbulent dissipation and turbulent kinetic energy increase. The most plausible reason is that the turbulent flow increases as the saturation pressure rises. The results of simulation results reveal that the distributions of turbulent dissipation

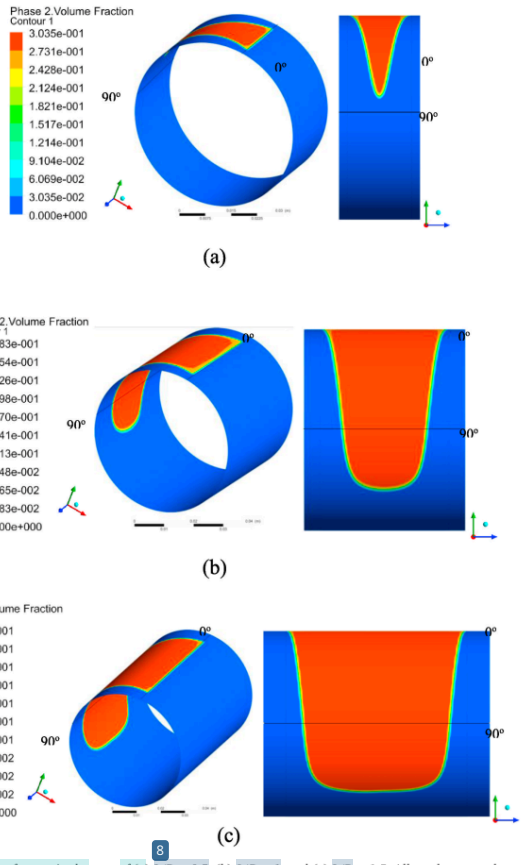

Fig 14. Contour of volume fraction of vapor in the case of (a) $L/D = 0.5$, (b) $L/D = 1$, and (c) $L/D = 1.5$. All results are evaluated on the stationary wall

rate at the middle-cross section of the bearing expand synchronously along with the turbulent kinetic energy profiles for all saturation pressure studied here. Based on Fig. 24, it can be highlighted that at a bearing angle of about 180°, the maximum values of turbulent kinetic energy and turbulent dissipation rate occur, which is similar to the profile of the acoustic power level shown in Fig. 24 (a). The local pressure drops dramatically and the velocity fluctuation rises as the lubricant passes the boundary marking the change from a rough to a smooth condition and is drawn into a diverging geometry between the surfaces. This could be the cause of the abrupt rise in turbulent kinetic energy or turbulent dissipation rate seen in Fig. 24 (b) and (c).

4.4. Effect of surface roughness level

In this section, the effect of surface roughness level on tribological, thermal and acoustic performance of journal bearing is of particular interest. The simulation results are conducted at the operational condition with length to diameter ratio (L/D) of 1, saturation pressure (P_{Sat}) of 30,000 Pa, and shaft rotational speed of 2000 rpm.

Fig. 25 shows the maximum pressure value generated by the heterogeneous rough/smooth journal bearing for several surface roughness levels R_a. Based on Fig. 25, it can be observed that the greater the roughness level R_a, the larger the maximum pressure P_{max}. The largest percentage increase in P_{max} occurs when the rough surface shifts from the "precision" (i.e. $R_a = 0.2$ μm in this case) to "fine" level (i.e. $R_a = 0.8$ μm). This percentage decreases as the roughened surface shifts from "medium" (i.e. $R_a = 3.2$ μm) to "rough" level (i.e. $R_a = 12.5$ μm). The highlight of the simulation results here is that the use of an engineered rough surface to create a heterogenous rough/smooth pattern for journal bearing has a positive effect in increasing the maximum pressure

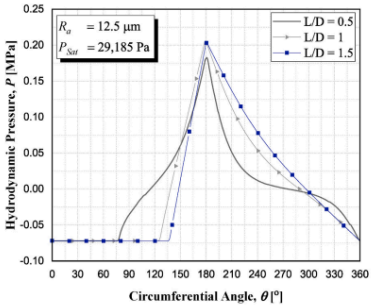

(a)

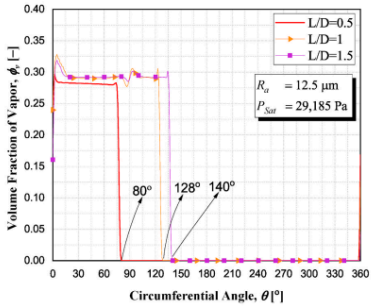

(b)

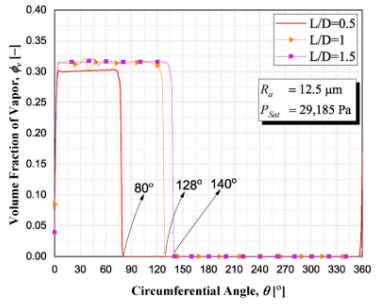

(c)

Fig. 15. Characteristics of (a) hydrodynamic pressure, (b) volume fraction of vapor evaluated on the stationary wall, and (c) volume fraction of vapor evaluated on the moving wall varying the length over diameter ratio (L/D). All results are evaluated at the mid-plane of the bearing ($z/L_b = 0.5$).

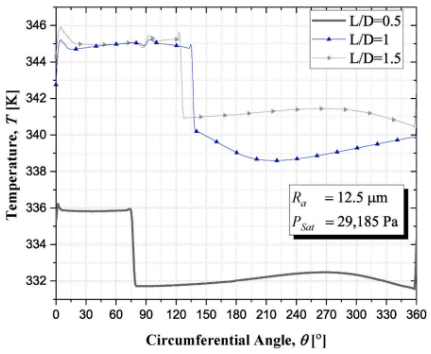

(a)

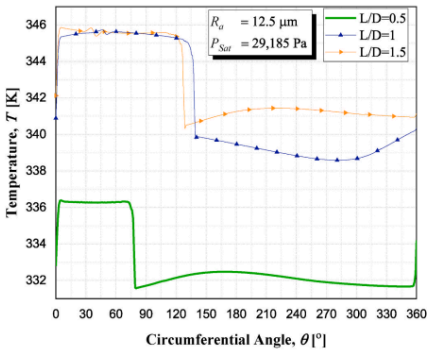

(b)

Fig. 16. Distribution of lubricant temperature evaluated on (a) stationary wall and (b) moving wall varying the length over diameter ratio (L/D). All results are evaluated at the mid-plane of the bearing ($z/L_b = 0.5$).

even when the concentric journal bearing is unable to generate pressure.

Concerning the effect of surface roughness level on the maximum temperature, Fig. 26 demonstrates that when the surface roughness level increases, the maximum temperature increases. It can be noted that the "rough" level (in this case $R_a = 15$ μm) of the surface gives the highest value of the maximum temperature. If compared to the "precision" level, it has increased by up to 9.81%. However, unlike the trend of increasing the maximum pressure, it is easy to see from Fig. 26 that the surface roughness has a relatively small influence on the film temperature. The main reason is that while increasing roughness raises pressure, it also creates a considerable increase in leak flow, which prevents the film temperature from rising.

To explore the effect of surface roughness level on tribological and acoustic performance, Fig. 27 shows the simulation results of load-carrying capacity, friction force, and average acoustic power level. In

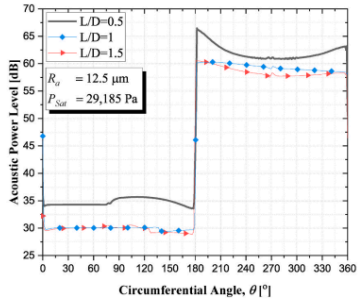

(a)

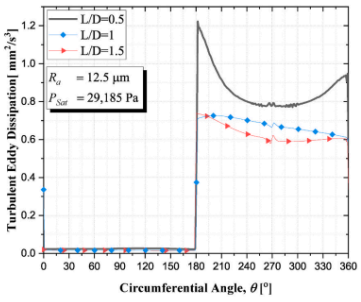

(b)

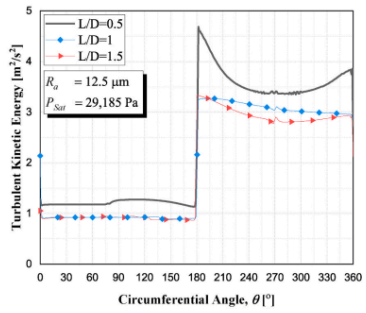

(c)

Fig. 17. Distribution of acoustic indices in terms of (a) acoustic power level, (b) turbulent eddy dissipation, and (c) turbulent kinetic energy varying the length over diameter ratio (L/D). All results are evaluated at the mid-plane of the bearing ($z/L_b = 0.5$).

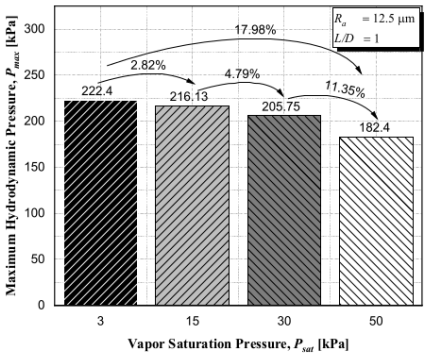

Fig. 18. Maximum pressure P_{max} as a function of the saturation pressure P_{sat}.

general, Fig. 27 (a) demonstrates that the load-carrying capacity of journal bearings increases with increasing surface roughness levels. This result is consistent with the findings of previously published research [22–26,50] indicating that surface roughness increases load-carrying capacity. It can also be seen based on Fig. 27 (a) that when the surface roughness level is designed as "rough", the load-carrying capacity has a positive value which means that the roughness with higher R_q is able to compensate for the magnitude of the external force. If the surface is roughened with the level of "precision" to "medium", the generated load-carrying capacity cannot compensate for the loading. This explains why the load-carrying capacity has a negative value. From the physical point of view, it indicates that the lubrication fails in the case of heterogeneous rough/smooth journal bearing with R_q = 0.2, 0.8, and 3.2 μm. In addition, Fig. 27 (b) and 27 (c) demonstrate that an increase in surface roughness level has the additional positive effects of reduced friction force and noise. For the case of heterogeneous rough/smooth with "rough" level, even with the concentric condition, the reduction in friction force and the noise level are calculated to be maximal. In conclusion, the roughness level of "rough", that is, $R_q \geq$ 12.5 μm is suitable to construct the heterogeneous rough/smooth journal bearing with high performance. This result is in line with the work of Ding et al. [51] who experimentally showed that using a micro-dimple on a surface can result in less friction compared to a smooth surface. Note that a micro-dimple is analogous to a large level of surface roughness as discussed here.

To investigate why, at zero eccentricity ratio, hydrodynamic action still occurs in terms of load support, it is necessary to comprehend the primary contributor to hydrodynamic pressure. In accordance with the classical theory of lubrication, the parallel slider cannot support the load due to the lack of a converging geometrical wedge to generate desirable hydrodynamic pressure. By constructing a heterogeneous bearing surface with roughness in some areas but not others, the flow pattern of the liquid lubricating surface can be modified. As a side note, the concept of heterogeneous rough/smooth bearing is analogous to the concept of heterogeneous slip/no-slip bearing, which, according to published works [23,30–32], can give rise to significant hydrodynamic pressure even under concentric conditions. The introduction of the roughness region can be viewed as a zone containing small geometrical local defects. These defects at the leading edge of the contact initiate the buildup of hydrodynamic pressure more quickly. In addition, it is demonstrated that roughness with a higher R_q appears to be able to generate a greater gradient pressure than roughness with a lower R_q (i.e. smoother surface). This roughness acts as a reservoir for lubricant, which can be

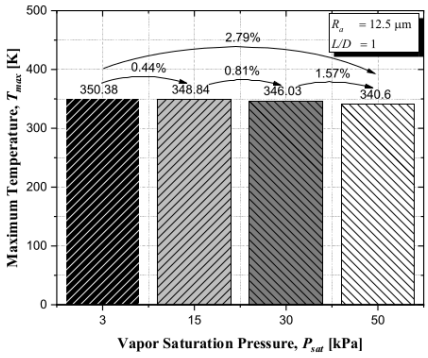

(a)

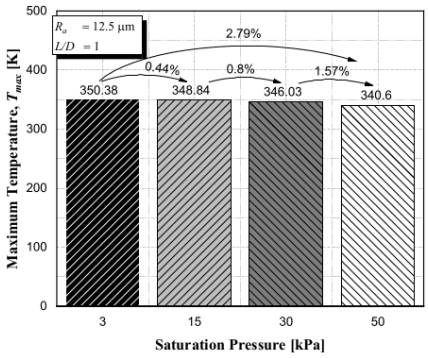

(b)

Fig. 19. Maximum lubricant temperature T_{max} as a function of the saturation pressure P_{sat} evaluated at (a) moving wall, (b) stationary wall.

advantageous for the lift-up. Henry et al. [52], who analyzed the behavior of polished and rough pad surfaces of two parallel surface thrust bearings, conducted an experiment that is consistent with the results presented here. In addition, the enhancement can be accomplished by employing a high texture density for partially textured designs, as was done in this study.

To determine the effect of the surface roughness level R_a on the cavitation phenomenon, the "cavitation area" indicator is presented in Fig. 28. It is cavitation area is evaluated for both moving and stationary walls. It can be seen in Fig. 28 that the cavitation area is formed only when the surface roughness of the journal bearing is at the medium (R_a = 3.2 μm) and rough (R_a = 12.5 μm and 15 μm) levels. When the surface roughness level is at the "precision" and "fine" level, the simulation results show that the cavitation area is zero. This is understandable because cavitation is not formed when μm is considered small enough to form a lubrication mechanism. It can be said that when R_a = 0.2 μm and

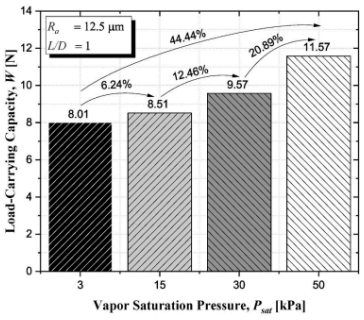

(a)

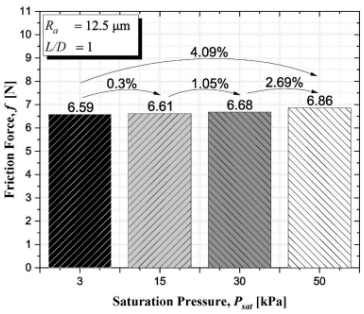

(b)

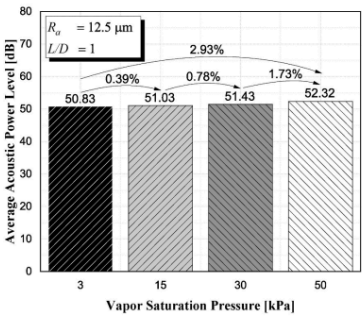

(c)

Fig. 20. Comparison of bearing performance with variation in vapor saturation pressure P_{sat} in terms of (a) load-carrying capacity, (b) friction force, and (c) average acoustic power level.

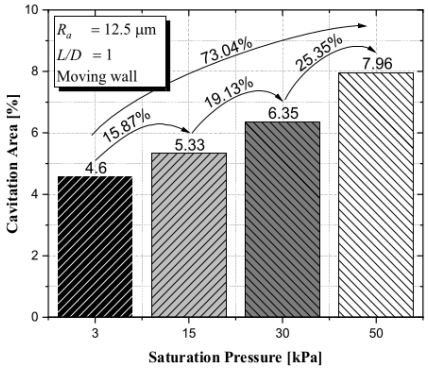

(a)

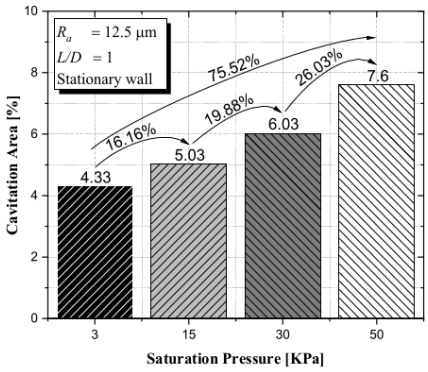

(b)

Fig. 21. Comparison of the cavitation area under varying saturation pressure which is evaluated on (a) the moving wall, and (b) the stationary wall.

0.8 μm, the lubrication has failed. Fig. 28 also reveals that the greater the level of surface roughness, the larger the possibility of cavitation.

Fig. 29 shows the distribution of hydrodynamic pressure and the volume fraction of vapor varying the surface roughness level R_a. Based on Fig. 29 (a), by analyzing the pressure distribution, it can be revealed that the maximum pressure at each surface roughness level variation occurs around 180°. Two specific features can be drawn from Fig. 29. Firstly, the larger the surface roughness level R_a, the longer the area of the lowest pressure. For example, the low-pressure area generated occurs in the circumferential angle ranges of 0°–102° (for R_a = 3.2 μm), 0°–126° (for R_a = 12.5 μm), and 0°–127° (for R_a = m). For cavitation to occur, these pressure drops must reach a value equal to the saturated vapor pressure. The distribution of the fraction volume of the vapor corresponding to the pressure profile is shown in Fig. 29 (b) and

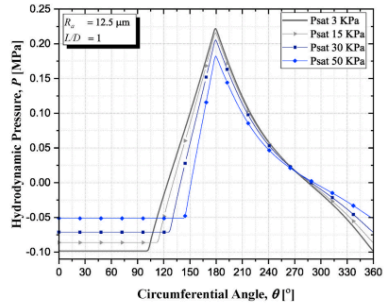

(a)

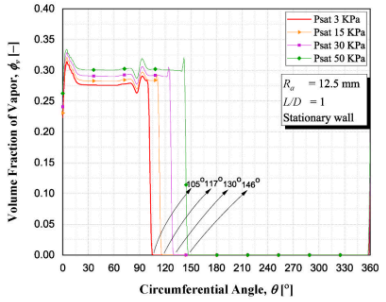

(b)

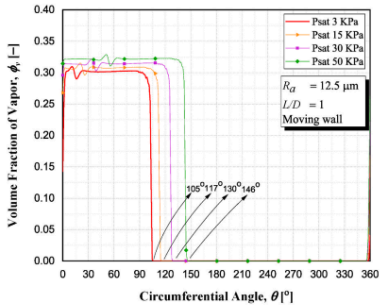

(c)

Fig. 22. Characteristics of (a) hydrodynamic pressure, (b) volume fraction of vapor evaluated at the stationary wall, and (c) volume fraction of vapor evaluated at the moving wall varying the saturation pressure P_{sat}. All results are evaluated at the mid-plane of the bearing (z/L_b = 0.5).

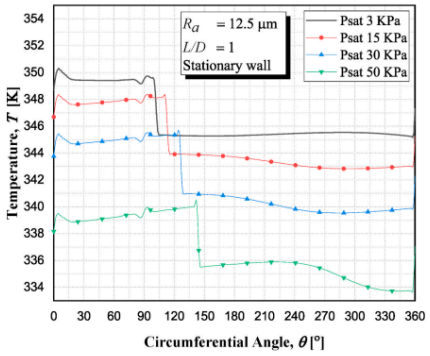

(a)

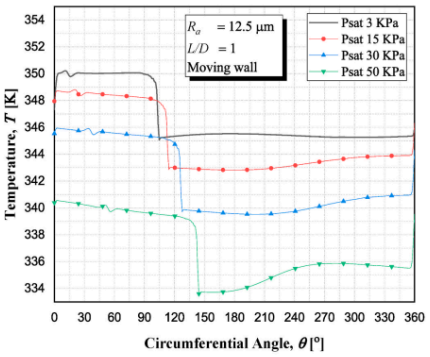

(b)

Fig. 23. Distribution of lubricant temperature varying saturation pressure P_{sat}, evaluated at (a) the moving wall, and (b) the stationary wall. All results are evaluated at the mid-plane of the bearing ($z/L_b = 0.5$).

(c). It was observed that the reformation of liquid takes place at the same location where pressure begins to rise from low pressure. Secondly, the pressure peak will increase as the surface roughness level increases. This result is in line with the result shown in Fig. 25. It can be also seen that for the surface roughness level R_a of 0.2 μm and 0.8 μm, there is no cavitation phenomenon. As discussed earlier, the lubrication fails. The surface roughness with a lower level is not able to generate the lubrication mechanism.

Fig. 30 shows the distribution of lubricant temperature varying surface roughness level R_a evaluated at (a) the moving wall, and (b) the stationary wall. Based on Fig. 30, it can be revealed that the temperature distribution becomes more pronounced as the surface roughness level increases. However, as stated in the previous discussion, for $R_a = 02$, 0.8, and 3.2 μm, journal bearing failure in lubrication is a result of

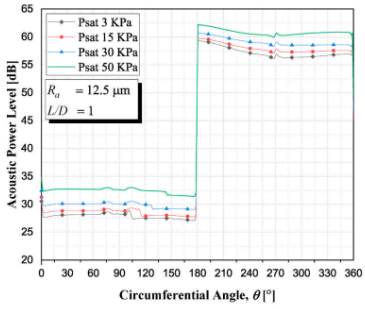

(a)

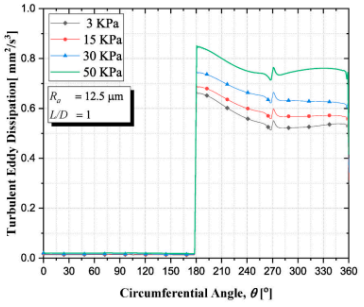

(b)

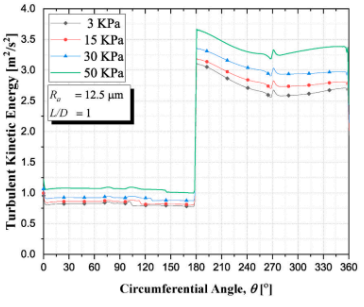

(c)

Fig. 24. Distribution of acoustic indices in terms of (a) acoustic power level, (b) turbulent eddy dissipation, and (c) turbulent kinetic energy varying the saturation pressure P_{sat}. All results are evaluated at the mid-plane of the bearing ($z/L_b = 0.5$).

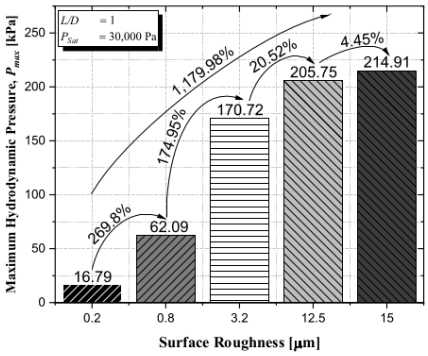

Fig. 25. Maximum pressure for several roughness levels R_a.

insufficient load-carrying capacity. The wedge effect, which is the dominant factor in generating pressure, is lost in this case because the eccentricity ratio ε is zero (concentric journal bearing). As a result, the lubricant temperature distribution is much lower in the low R_a case than when the surface condition is rough (i.e. $R_a = 12$ μm). It is intriguing to note that the temperature value calculated at the stationary and moving wall areas peaks at the same circumferential angle range (i.e. θ = 0°–10°). When the lubricant temperature at the stationary wall reaches its peak, however, the trend diverges in accordance with the trend of the temperature at the moving wall. This is because of the (partial) surface roughness boundary conditions at 0°–180° in the stationary wall region of the journal bearing.

In order to thoroughly analyze the properties of the journal bearing, in addition to the tribological performance stated before, the effect of the surface roughness level on the related acoustic indices must be investigated. Fig. 31 show the distribution of acoustic indices in terms of (a) acoustic power level, (b) turbulent eddy dissipation, and (c) turbulent kinetic energy varying the surface roughness level R_a. Based on Fig. 31 (a), it can be seen that the distribution of acoustic power level decreases as the surface roughness level increases. At the same level of surface roughness, which in this case is rough, the acoustic power distribution is also at the same level. The simulation test results reveal that the distribution of turbulent dissipation rate at the middle cross-section of the bearing expands synchronously with turbulent kinetic energy profiles for all surface roughness levels investigated in this study. Present numerical studies indicate that the profiles of acoustical indices in the divergent region of roughened journal bearings are significantly higher than those in the convergent region. This is understandable because the employment of a roughened surface with a lower R_a causes the surface acoustic power level to fluctuate more dramatically than one with a higher R_a.

5. Conclusions

Through computational fluid dynamics (CFD) procedures, the paper presented a detailed study of the acoustic, thermal, and tribological performance indices of heterogeneous rough/smooth journal bearings in concentric conditions. To capture the phenomenon more accurately, a thermo-hydrodynamic analysis with multiphase change boundary condition was used. In this study, the effects of length-to-diameter (L/D) ratio, vapor saturation pressure (P_{sat}), and surface roughness level (R_a) on bearing performance indicators were examined.

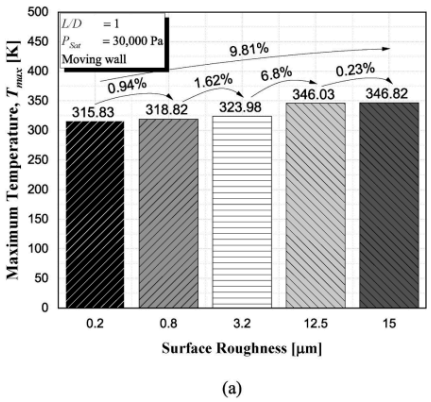

Fig. 26. Maximum lubricant temperature T_{max} as a function of the surface roughness level R_a evaluated for (a) moving wall, and (b) stationary wall.

1. The length-over-diameter ratio (L/D) has a significant effect on the tribological, thermal, and acoustic performance of the journal bearings. By increasing the L/D, the peak hydrodynamic pressure and consequently the load-carrying capacity can be increased. In addition, increasing the L/D can slightly increase the maximum lubricant temperature, while decreasing the acoustic power level slightly and significantly increasing the friction force.
2. The surface roughness level of the heterogeneous rough/smooth pattern should be constructed as a "rough" surface with R_a greater than 12.5 μm for maximum bearing performance. Such a roughened surface generates a high load-carrying capacity, enabling the lubricating performance to be effective even under intense conditions.
3. For a hydrodynamic heterogeneous rough/smooth journal bearing with a high level of surface roughness, the study confirmed that the variation of vapor saturation pressure does not change very much the

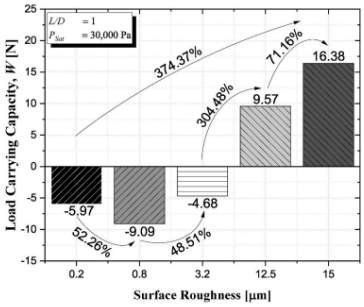

(a)

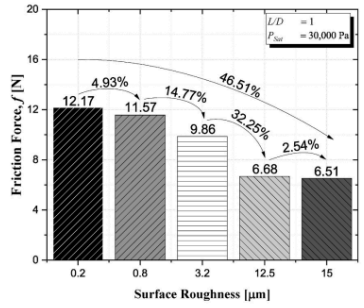

(b)

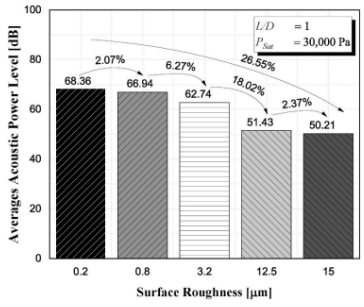

(c)

Fig. 27. Comparison of bearing performance with variation in surface roughness level R_a in terms of (a) load-carrying capacity, (b) friction force, and (c) average acoustic power level.

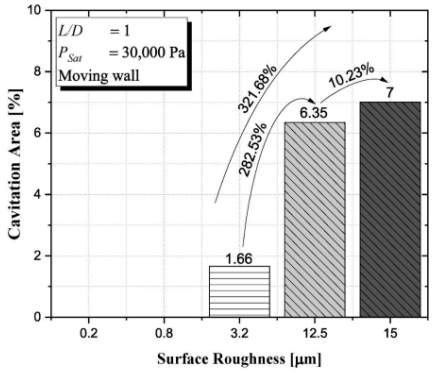

(a)

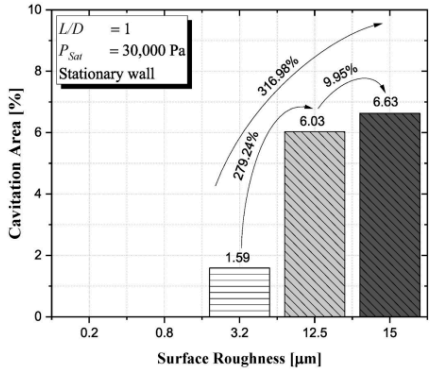

(b)

Fig. 28. Characteristics of cavitation area evaluated for (a) the moving wall, and (b) the stationary wall varying the surface roughness level R_a.

maximum temperature (<3%), the friction force (<5%) and the noise level (<3%). Furthermore, it was found that the load-carrying capacity increases with the saturation pressure.

Funding: This research is fully funded by University of Diponegoro through WCRU Grant, No. 118–13/UN7.6.1/PP/2021.

Declaration of competing interest

The authors declare that they have no known competing financial interests or personal relationships that could have appeared to influence the work reported in this paper.

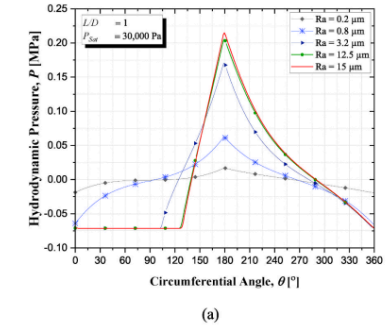

(a)

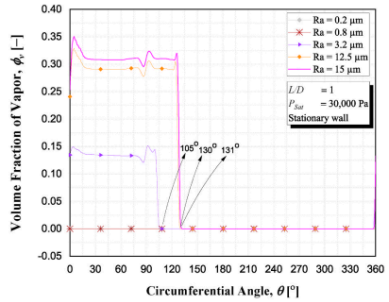

(b)

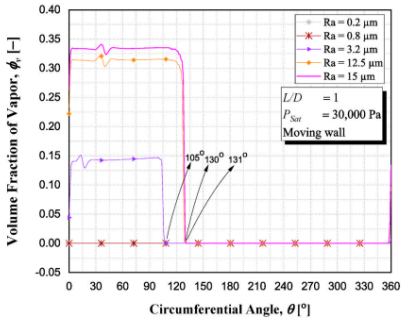

(c)

Fig. 29. Distribution of lubricating characteristics varying the surface roughness level R_a in terms of (a) hydrodynamic pressure, (b) volume fraction of vapor evaluated at the moving wall, and (c) volume fraction of vapor evaluated at the stationary wall. All results are evaluated at the mid-plane of the bearing ($z/L_b = 0.5$).

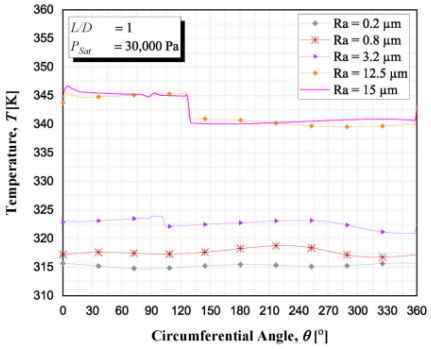

(a)

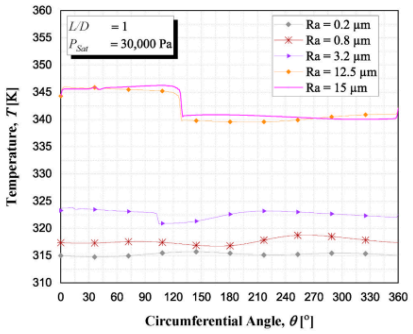

(b)

Fig. 30. Distribution of lubricant temperature varying surface roughness level R_a evaluated at (a) the moving wall, and (b) the stationary wall. All results are evaluated at the mid-plane of the bearing ($z/L_b = 0.5$).

Data availability

Data will be made available on request.

Nomenclature

c	Radial clearance, mm
C_p	Specific heat capacity, J/kg·K
D_j	Journal diameter, mm
D_b	Bearing diameter, mm
f	Friction force, N
k	Turbulent kinetic energy, m^2/s^2
K_s	Roughness height, mm
L_b	Length of the bearing, mm
L_{cj}	Circumferential length of the bearing, mm
L_R	Length of roughness area, mm

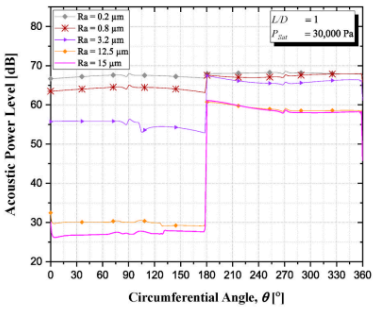

(a)

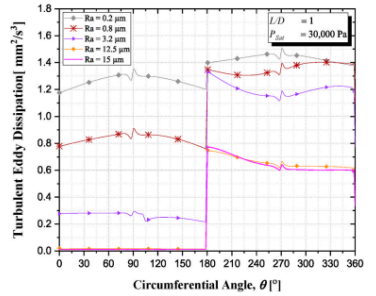

(b)

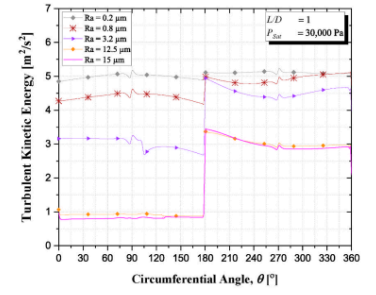

(c)

Fig. 31. Distribution of acoustic indices varying the surface roughness level R_a in terms of (a) acoustic power level, (b) turbulent eddy dissipation, and (c) turbulent kinetic energy. All results are evaluated at the mid-plane of the bearing ($z/L_b = 0.5$).

n	Rotational speed, rpm
O_b	Bearing center, mm
O_j	Journal center, mm
p	Hydrodynamic pressure, Pa
P_{AL}	Average acoustic power level, dB
P_{sat}	Oil vapor saturation pressure, Pa
R_a	Roughness average, μm
R_b	Bearing radius, mm
R_B	Bubble radius, mm
R_g, R_c	Mass transfer rate between the liquid and vapor phases in cavitation
R_j	Journal radius, mm
T	Temperature, K
W_R	Roughness width, mm
W	Load-carrying capacity, N
ε_d	Turbulent dissipation rate, mm^2/s^3
ε	Eccentricity ratio
λ	Thermal conductivity, W/m·K
μ_o	Oil viscosity, Pa. S
μ_v	Oil vapor viscosity, Pa. S
ν	Kinematic viscosity, m^2/s
ρ	Oil liquid density, kg/m^3
ρ_v	Oil vapor density, kg/m^3
φ	Attitude angle (°)
θ	Circumferential angle (°)

References

[1] D.Y. Dhande, D.W. Pande, Multiphase flow analysis of hydrodynamic journal bearing using CFD coupled fluid structure interaction considering cavitation, J. King Saud Univ. Eng. Sci. 30 (4) (2018) 345–354, https://doi.org/10.1016/j.jksues.2016.09.001.

[2] X. Zhang, Z. Yin, G. Gao, Z. Li, Determination of stiffness coefficients of hydrodynamic water-lubricated plain journal bearings, Tribol. Int. 85 (2015) 37–47, https://doi.org/10.1016/j.triboint.2014.12.019.

[3] X. Zhang, Z. Yin, D. Jiang, G. Gao, Y. Wang, X. Wang, Load carrying capacity of misaligned hydrodynamic water-lubricated plain journal bearings with rigid bush materials, Tribol. Int. 99 (2016) 1–13, https://doi.org/10.1016/j.triboint.2016.02.038.

[4] K. Maharshi, T. Mukhopadhyay, B. Roy, L. Roy, S. Dey, Stochastic dynamic behaviour of hydrodynamic journal bearings including the effect of surface roughness, Int. J. Mech. Sci. 142 (143) (2018) 370–383, https://doi.org/10.1016/j.ijmecsci.2018.04.012.

[5] Q. Lin, Z. Wei, N. Wang, W. Chen, Effect of large-area texture/slip surface on journal bearing considering cavitation, Ind. Lubric. Tribol. 67 (3) (2015) 216–226, https://doi.org/10.1108/ILT-05-2013-0055.

[6] Y. Hori, Hydrodynamic Lubrication, Springer, Tokyo, 2006, https://doi.org/10.1007/4-431-27901-6.

[7] Y. Mao, L. Zeng, Y. Lu, Modeling and optimization of cavitation on a textured cylinder surface coupled with the wedge effect, Tribol. Int. 104 (2016) 212–224, https://doi.org/10.1016/j.triboint.2016.09.002.

[8] D. Bulut, N. Bader, G. Poll, Cavitation and film formation in hydrodynamically lubricated parallel sliders, Tribol. Int. 162 (2021), 107113, https://doi.org/10.1016/j.triboint.2021.107113.

[9] Y. Chen, Y. Sun, Q. He, J. Feng, Elastohydrodynamic behavior analysis of journal bearing using fluid–structure interaction considering cavitation, Arabian J. Sci. Eng. 44 (2) (2019) 1305–1320, https://doi.org/10.1007/s13369-018-3467-9.

[10] D.Y. Dhande, D.W. Pande, A two-way FSI analysis of multiphase flow in hydrodynamic journal bearing with cavitation, J. Braz. Soc. Mech. Sci. Eng. 39 (2017) 3399–3412, https://doi.org/10.1007/s40430-017-0750-8.

[11] B.A. Abass, S.Y. Ahmed, Z.H. Kadhim, Thermoelasto-hydrodynamic analysis of nano-lubricated journal bearings using computational fluid dynamics with two-way fluid–structure interaction considering cavitation, Arabian J. Sci. Eng. 48 (2023) 2939–2950, https://doi.org/10.1007/s13369-022-07024-9.

[12] N.J. Morris, H. Shahmohamadi, R. Rahmani, A. Rahnejat, C.P. Garner, Combined experimental and multiphase computational fluid dynamics analysis of surface textured journal bearings in mixed regime of lubrication, Lubric. Sci. 30 (2018) 161–173, https://doi.org/10.1002/ls.1414.

[13] D. Sun, S. Li, C. Fei, Y. Ai, R. P, Liem Investigation of the effect of cavitation and journal whirl on static and dynamic characteristics of journal bearing, J. Mech. Sci. Technol. 33 (1) (2019) 77–86, https://doi.org/10.1007/s12206-018-1208-3.

[14] J. Yang, A. Palazzolo, Three-dimensional thermo-elasto-hydrodynamic computational fluid dynamics model of a tilting pad journal bearing - Part I: static response, J. Tribol. 141 (6) (2019) 61702–61709, https://doi.org/10.1115/1.4043349.

[15] Y. Chen, J. Feng, Y. Sun, X. Peng, Q. Dai, C. Yu, Effect of groove shape on the hydrodynamic lubrication of journal bearing considering cavitation, Eng. Comput.

37 (5) (2020) 1557–1576. https://doi-org.proxy.undip.ac.id/10.1108/EC-06-2019-0287.
[16] Y. Chen, X. Shi, X. Wang, H. Wang, C. Yu, Y. Sun, Multi-objective analysis design of spiral groove conical bearing considering cavitation effects, Results Eng 15 (2022), 100582, https://doi.org/10.1016/j.rineng.2022.100582.
[17] Q. Li, S. Zhang, Y. Wang, W.W. Xu, Z. Wang, Investigations of the three-dimensional temperature field of journal bearings considering conjugate heat transfer and cavitation, Ind. Lubric. Tribol. 71 (1) (2019) 109–118, https://doi.org/10.1108/ILT-03-2018-0113.
[18] M.E. Kyrkou, P.G. Nikolakopoulos, Simulation of thermo-hydrodynamic behavior of journal bearings, lubricating with commercial oils of different performance, Simulat. Model. Pract. Theor. 104 (2020), 102128, https://doi.org/10.1016/j.simpat.2020.102128.
[19] G. Xiang, T. Yang, J. Guo, J. Wang, B. Liu, S. Chen, Optimization transient wear and contact performances of water-lubricated bearings under fluid-solid-thermal coupling condition using profile modification, Wear 502– 503 (2022), 204379, https://doi.org/10.1016/j.wear.2022.204379.
[20] K.J. Stout, W.B. Rowe, Externally pressurised bearings - design for manufacture, Part 1, Tribol. Int. 7 (1974) 98–106, https://doi.org/10.1016/0041-2678(74)90009-8.
[21] R.L. Paiva, D. Oliveira, R.S. Ruzzi, M.J. Jackson, R.V. Gelamo, A.M. Abrão, R. B. Silva, Surface roughness and morphology evaluation of bearing steel after grinding with multilayer graphene platelets dispersed in different base fluids, Wear 523 (2023) (2023), 204852, https://doi.org/10.1016/j.wear.2023.204852.
[22] S.U. Bhaskar, M.M. Hussain, M.Y. Ali, Stability analysis on plain journal bearing with effect of surface roughness, Int. J. Sci. Eng. Res. 4 (2013) 1–8.
[23] G.K. Kalavathi, P.A. Dinesh, K. Gururajan, Influence of roughness on porous finite journal bearing with heterogeneous slip/no-slip surface, Tribol. Int. 102 (2016) 174–181, https://doi.org/10.1016/j.triboint.2016.05.032.
[24] B. Yin, H. Zhou, B. Xu, H. Jia, The influence of roughness distribution characteristic on the lubrication performance of textured cylinder liners, Ind. Lubric. Tribol. 71 (3) (2019) 486–493, https://doi.org/10.1108/ILT-07-2018-0258.
[25] S. Zhu, J. Sun, B. Li, G. Zhu, Thermal turbulent lubrication analysis of rough surface journal bearing with journal misalignment, Tribol. Int. 144 (2020), 106109, https://doi.org/10.1016/j.triboint.2019.106109.
[26] D. Skaltsas, G.N. Rossopoulos, C.I. Papadopoulos, A comparative study of the Reynolds equation solution for slider and journal bearings with stochastic roughness on the stator and the rotor, Tribol. Int. 167 (2022), 107410, https://doi.org/10.1016/j.triboint.2021.107410.
[27] A.K. Tomar, S.C. Sharma, Study on surface roughness and piezo-viscous shear thinning lubricant effects on the performance of hole-entry hybrid spherical journal bearing, Tribol. Int. 168 (2022), 107349, https://doi.org/10.1016/j.triboint.2021.107349.
[28] N. Baineni, N. Borse, N.S. Chippa, Analysis of thermoelastohydrodynamic lubrication of journal bearing including the effect of surface roughness and cavitation, J. Inst. Eng. India Ser. D (2022), https://doi.org/10.1007/s40033-022-00335-z.
[29] M. O Othman, A.H. Elkholy, A.A. Seireg, Experimental investigation of frictional noise and surface-roughness characteristics, Exp. Mech. 30 (1990) 328–331, https://doi.org/10.1007/BF02321499.
[30] G.J. Ma, C.W. Wu, P. Zhou, Wall slip and hydrodynamics of two-dimensional journal bearing, Tribol. Int. 40 (7) (2007) 1056–1066, https://doi.org/10.1016/j.triboint.2006.10.003.
[31] S. Cui, C. Zhang, M. Fillon, L. Gu, Optimization performance of plain journal bearings with partial wall slip, Tribol. Int. 145 (2020), 106137, https://doi.org/10.1016/j.triboint.2019.106137.
[32] M. Tauviqirrahman, J. Jamari, S. Susilowati, C. Pujiastuti, B. Setiyana, A. H. Pasaribu, M. I Ammarullah, Performance comparison of Newtonian and non-Newtonian fluid on a heterogeneous slip/no-slip journal bearing system based on CFD-FSI method, Fluid 7 (2022) 225, https://doi.org/10.3390/fluids7070225.
[33] F. Meng, R. Shu, L. Chen, Influences of operation parameters on noise of journal bearing with compound texture considering lubricant thermal effect, Proc. Inst. Mech. Eng. Part J: J. Eng. Tribol. 234 (7) (2020) 991–1006, https://doi.org/10.1177/1350650119868910.
[34] R.J. Welsh, Plain Bearing Design Handbook, first ed., Butterworths, London, 1983.
[35] G. Gao, Z. Yin, D. Jiang, X. Zhang, Numerical analysis of plain journal bearing under hydrodynamic lubrication by water, Tribol. Int. 75 (2014) 31–38, https://doi.org/10.1016/j.triboint.2014.03.009.
[36] ANSYS, ANSYS Fluent, Version 16.0: Theory Guide, ANSYS, Inc., Canonsburg, USA, 2017.
[37] B.E. Launder, D.B. Spalding, Lectures in Mathematical Models of Turbulence, Academic Press, London, 1972.
[38] M.S. Rubio, F.C. Castillo, F.R. Aquino, J.L. Romero, A new focus on the Walther equation for lubricant viscosity determination, Lubric. Sci. 18 (2006) 95–107, https://doi.org/10.1002/ls.9.
[39] H. Kamat, C.R. Kini, S.B. Shenoy, Effect of cavitation and temperature on fluid film bearing using CFD and FSI technique: a Review, Arch. Comput. Methods Eng. 30 (2023) 1623–1636, https://doi.org/10.1007/s11831-022-09847-z.
[40] T. Adams, C. Grant, H. Watson, A simple algorithm to relate measured surface roughness to equivalent sand-grain roughness, Int. J. Mech. Eng. Mechatron. 1 (1) (2012) 66–71, https://doi.org/10.11159/ijmem.2012.008.
[41] E. Croner, O. Léon, F. Chedevergne, Industrial use of equivalent sand grain height models for roughness modelling in turbomachinery, in: 55th 3AF International Conference on Applied Conference, 2021, p. Apr.
[42] Japanese Industrial Standard/Japanese Standards Association. JIS B 0601:2013 Geometrical Product Specifications (GPS) –, Surface Texture: Profile Method – Terms, Definitions and Surface Texture Parameters, Foreign Standard), January, 2013.
[43] M.J. Braun, W.M. Hannon, Cavitation formation and modelling for fluid film bearings: a review, Proc. Inst. Mech. Eng. Part J: J. Eng. Tribol. 224 (9) (2010) 839–863, https://doi.org/10.1243/13506501JET77.
[44] D. Sun, C. Zhang, R. Guo, J.G. Yang, Solution of dynamic characteristics of journal bearing based on two-phase flow theory, J. Aero. Power 27 (12) (2012) 2821–2827.
[45] P. Zwart, A. Gerber, T. Belamri, A two-phase flow model for predicting cavitation dynamics, Yokohama, Japan, May 30-June 3, in: Fifth Int. Conf. Multiph. Flow (ICMF), 2004.
[46] T.G. Leighton, Derivation of the Rayleigh–Plesset Equation in Terms of Volume, Institute of Sound and Vibration Research, Southampton, UK, 2007.
[47] M. Lilley, The Radiated Noise from Isotropic Turbulence Revisited. NASA Contract Report, vols. 93–75, NASA Langley Research Center, Hampton, VA, 1993.
[48] F. Meng, Z. Wei, D. Minggang, G. Gao, Study of acoustic performance of textured journal bearing, Proc. Inst. Mech. Eng. Part J: J. Eng. Tribol. 230 (2) (2016) 156–169, https://doi.org/10.1177/1350650115594406.
[49] D. Littlejohn, D. Lucas, Vapor pressure measurement system for heavy crude oils, J. Air Waste Manag. Assoc. 49 (9) (1999) 1103–1109, https://doi.org/10.1080/10473289.1999.10463876.
[50] T. Nagaraju, S.C. Sharma, S.C. Jain, Influence of surface roughness effects on the performance of nonrecessed hybrid journal bearings, Tribol. Int. 35 (2002) 467–487, https://doi.org/10.1016/S0301-679X(02)00037-3.
[51] S. Ding, J. Xu, P. Liu, Z. Shi, O. Yang, Y. Hu, Geometric influence on friction and wear performance of cast iron with a micro-dimpled surface, Results Eng 9 (2021), 100211, https://doi.org/10.1016/j.rineng.2021.100211.
[52] Y. Henry, J. Bouyer, M. Fillon, Experimental analysis of the hydrodynamic effect during start-up of fixed geometry thrust bearings, Tribol. Int. 120 (2018) 299–308, https://doi.org/10.1016/j.triboint.2017.12.021.

Investigation on acoustic, thermal, and tribological properties of hydrodynamic journal bearing with heterogeneous rough/smooth surface

ORIGINALITY REPORT

14%	14%	%	4%
SIMILARITY INDEX	INTERNET SOURCES	PUBLICATIONS	STUDENT PAPERS

PRIMARY SOURCES

1	Submitted to University of California, Merced Student Paper	1%
2	opus4.kobv.de Internet Source	1%
3	semarakilmu.com.my Internet Source	1%
4	www.researchgate.net Internet Source	1%
5	www.scopus.com Internet Source	1%
6	es.scribd.com Internet Source	1%
7	Submitted to Universitas Diponegoro Student Paper	1%
8	www.ideals.illinois.edu Internet Source	<1%
9	Submitted to Queensland University of Technology Student Paper	<1%
10	123dok.net Internet Source	<1%
11	www.pmt.usp.br Internet Source	<1%
12	www.tribology.rs Internet Source	<1%

13	static.frontiersin.org Internet Source	<1 %
14	Submitted to City University Student Paper	<1 %
15	sam.ensam.eu Internet Source	<1 %
16	ebin.pub Internet Source	<1 %
17	spiral.imperial.ac.uk Internet Source	<1 %
18	daneshyari.com Internet Source	<1 %
19	researchmgt.monash.edu Internet Source	<1 %
20	www.scribd.com Internet Source	<1 %
21	www.tribomat.net Internet Source	<1 %
22	assets-eu.researchsquare.com Internet Source	<1 %
23	iopscience.iop.org Internet Source	<1 %
24	pure.tue.nl Internet Source	<1 %
25	Submitted to University of Technology, Jamaica Student Paper	<1 %
26	kepakaran.apps.undip.ac.id Internet Source	<1 %
27	mdpi-res.com Internet Source	<1 %
28	www.emeraldinsight.com Internet Source	<1 %

29	www.thermo-a.mw.tu-muenchen.de Internet Source	<1 %
30	www.espublisher.com Internet Source	<1 %
31	hal.archives-ouvertes.fr Internet Source	<1 %
32	Submitted to Higher Education Commission Pakistan Student Paper	<1 %
33	ensias.um5.ac.ma Internet Source	<1 %
34	Submitted to University of Mosul Student Paper	<1 %
35	dokumen.pub Internet Source	<1 %
36	pt.scribd.com Internet Source	<1 %
37	dl.cfdexperts.net Internet Source	<1 %
38	pubs.aip.org Internet Source	<1 %
39	uwspace.uwaterloo.ca Internet Source	<1 %
40	www.econstor.eu Internet Source	<1 %
41	publikationen.bibliothek.kit.edu Internet Source	<1 %
42	www.diagnostyka.net.pl Internet Source	<1 %
43	www.icevirtuallibrary.com Internet Source	<1 %
44	dspace.dtu.ac.in:8080 Internet Source	

		<1 %
45	journal.iistr.org Internet Source	<1 %
46	journals-jd.upm.edu.my Internet Source	<1 %
47	ksme.or.kr Internet Source	<1 %
48	link.springer.com Internet Source	<1 %
49	m.moam.info Internet Source	<1 %
50	publikationen.sulb.uni-saarland.de Internet Source	<1 %
51	pustaka.sttw.ac.id Internet Source	<1 %
52	real.mtak.hu Internet Source	<1 %
53	scindeks-clanci.ceon.rs Internet Source	<1 %
54	tessera.spandidos-publications.com Internet Source	<1 %
55	www.cell.com Internet Source	<1 %
56	www.diva-portal.org Internet Source	<1 %
57	www.hindawi.com Internet Source	<1 %
58	www.ijser.org Internet Source	<1 %
59	www.jafmonline.net Internet Source	<1 %

60	www.mdpi.com Internet Source	<1 %
61	www.tandfonline.com Internet Source	<1 %
62	www.ukessays.com Internet Source	<1 %
63	www2.mdpi.com Internet Source	<1 %

Exclude quotes	Off	Exclude matches	Off
Exclude bibliography	On		

Investigation on acoustic, thermal, and tribological properties of hydrodynamic journal bearing with heterogeneous rough/smooth surface

GRADEMARK REPORT

FINAL GRADE

/100

GENERAL COMMENTS

PAGE 1

PAGE 2

PAGE 3

PAGE 4

PAGE 5

PAGE 6

PAGE 7

PAGE 8

PAGE 9

PAGE 10

PAGE 11

PAGE 12

PAGE 13

PAGE 14

PAGE 15

PAGE 16

PAGE 17

PAGE 18

PAGE 19

PAGE 20

PAGE 21

PAGE 22